UNIVERSITAT DE BARCELONA
DEPARTAMENT D'ASTRONOMIA I METEOROLOGIA

UNIVERSITAT DE BARCELONA

U
B

Determination of the distance to the Andromeda Galaxy using variable stars

Memòria presentada per
Francesc Vilardell Sallés
per optar al grau de
Doctor en Física

Barcelona, gener de 2009

4 Eclipsing binaries⋆

Five of the 24 EBs selected as suitable distance indicators (Sect 2.4.1) were observed with GMOS at Gemini-North (Sect. 3.1.1). The preliminary analysis performed (Sect. 2.4.1) indicates that two of the observed targets are optimum for obtaining a precise distance determination to M 31: M31V J00443799+4129236 and M31V J00443610+4129194. Therefore, both EBs were modeled in order to determine the physical properties of their components (Sect. 4.1) and to derive a direct distance to M 31 (Sect. 4.2). Two of the other observed targets have some particular characteristics that diminish their value for distance determination. One of them is a single-line EB (M31V J00444528+4128000) and the other one has a strong third light contribution (M31V J00442326+4127082). In spite of that, these EBs were also modeled in order to constrain the fundamental properties of massive stars in M 31 (Sect. 4.1). The fifth target observed with GMOS (M31V J00445011+4128069) is the faintest target in Table 2.3 and, after thorough investigation, no meaningful results could be obtained because of the low signal-to-noise ratio (S/N) of the obtained spectra (Table 3.2). Therefore, future observations with a larger telescope are required for this target.

In order to facilitate the identification to the reader, shorter identifiers have been used to refer to the four analyzed EBs (Table 4.1). According to the number of system components, the two double-line EBs have been referred to as SB2A and SB2B, the single-line EB as SB1 and the triple-line EB as SB3.

Table 4.1. Equivalence between the identifier in the variable star catalog and the shorter name given in the course of the present chapter.

M31V J00443799+4129236	SB2A
M31V J00443610+4129194	SB2B
M31V J00444528+4128000	SB1
M31V J00442326+4127082	SB3

⋆Part of the contents of this chapter were published in Ribas et al. (2005).

4.1 Physical properties

As in the case of the selection of targets (Sect. 2.4.1), each EB needs to be modeled as a particular case and a specific approach was followed for each one of them. In general, the treatment of all the targets consists of the following steps:

- Acquisition of RVs from the observed spectra,

- Determination of the masses and radii of the components from the modeling of the light and the RV curves,

- Determination of the temperature of the components and line-of-sight absorption, and

- Comparison with stellar evolutionary models.

The detailed approach used for each one of the four studied targets is explained below.

4.1.1 M31V J00443799+4129236 (SB2A)

4.1.1.1 Radial velocities

For double-line EBs, RV determinations involve the precise determination of the center of the (usually) blended spectral lines. To derive RVs of these stars, we considered several approaches on both spectral disentangling and two-dimensional cross-correlation. We carried out numerous tests with the spectral disentangling codes TANGLE (Harries et al., 2003) and KOREL (Hadrava, 1995), and considering different wavelength intervals. Using a grid search method we observed that the obtained solutions had a relatively large spread and it was not possible to establish a definitive solution because of the noisy χ^2 surface.

Alternatively, we used the TODCOR two-dimensional cross-correlation algorithm (Zucker & Mazeh, 1994). We calculated individual RVs for each spectrum by cross-correlating with synthetic templates from Kurucz ATLAS9 models[1] and the TLUSTY libraries (OSTAR2002 and BSTAR2006) of Lanz & Hubeny (2003, 2007)[2]. In both sets of models we considered templates with solar metallicity, different temperatures and gravities (Fig. 4.1), and rotational velocities in steps of 40 km s^{-1}, starting at 80 km s^{-1} (the wavelength resolution of the spectra is $\sim$ 80 km s^{-1}). The microturbulent velocity was set to 2 km s^{-1} for the ATLAS9 and BSTAR2006 models and to 10 km s^{-1} for the OSTAR2002 models, since these velocity values provide the maximum temperature and gravity coverage.

---

[1]Available at: `http://kurucz.cfa.harvard.edu/`
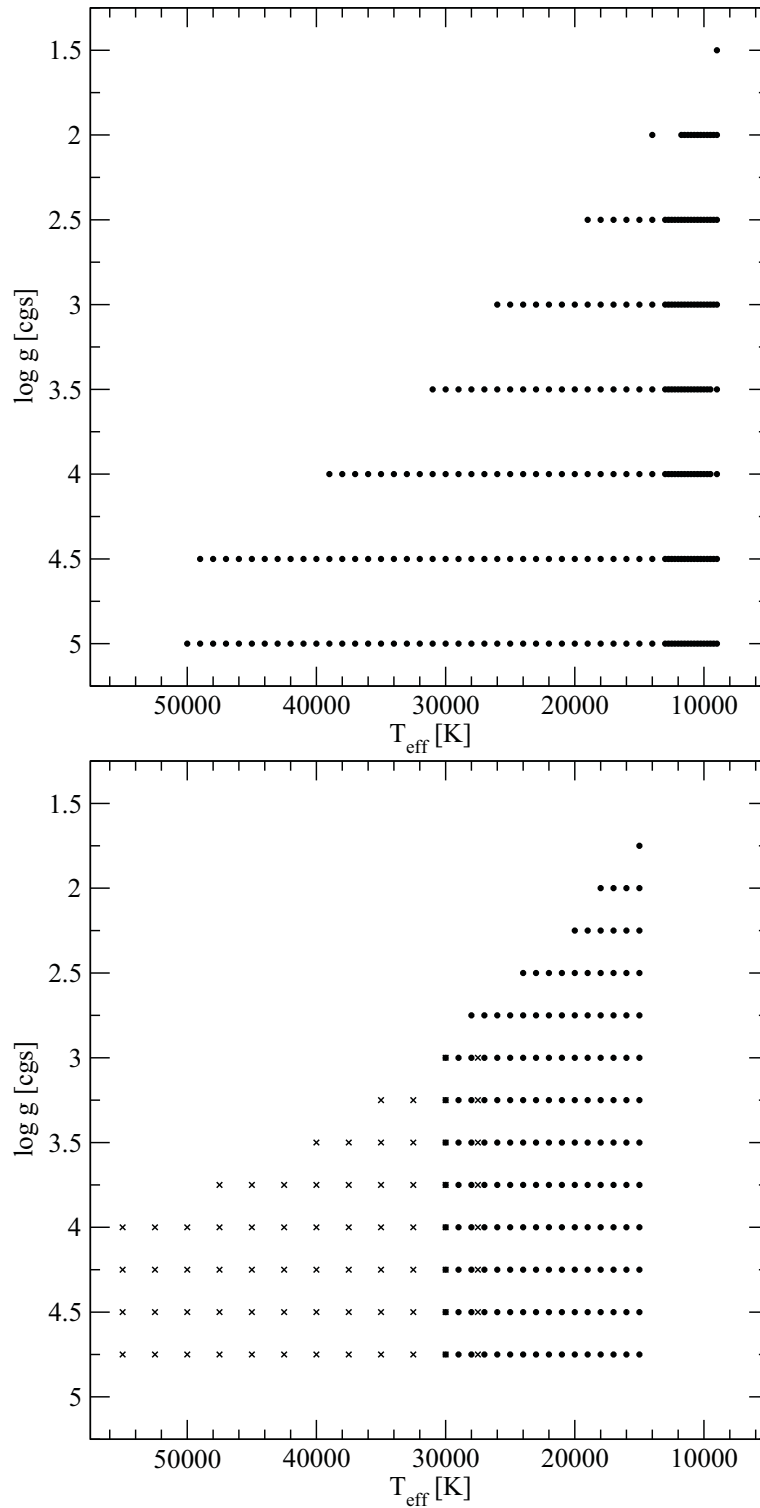[2]Available at: `http://nova.astro.umd.edu/`

Figure 4.1. Effective temperature and gravity coverage for the two sets of models used for RV determination. **Top:** Kurucz ATLAS9 models. **Bottom:** TLUSTY OSTAR2002 (crosses) and BSTAR2006 models (circles).

Table 4.2. Radial velocity determinations for the EB M31V J00443799+4129236 (SB2A).

Time	Phase	Primary	Secondary
[HJD]		[km s^{-1}]	[km s^{-1}]
2 453 262.874	0.1812	-338.1± 7.5	88.4± 7.5
2 453 319.879	0.2403	-349.1± 7.6	116.4± 6.2
2 453 260.910	0.6278	-52.9±10.8	-382.0±11.7
2 453 321.820	0.7871	10.5±13.9	-426.4±10.2
2 453 321.872	0.8016	-1.1± 9.3	-417.9± 8.6

The RVs obtained with TODCOR depend on the pair of synthetic templates used. Given the huge number of possible pairs of models resulting from the TLUSTY and ATLAS9 grids, two different procedures were used to determine the pair of models providing the best synthetic templates. The first procedure used the values derived from the light curve fitting (Sect. 2.4.1) and the observed colors ($B - V$) to determine preliminary temperatures, surface gravities and rotational velocities for an initial pair of models. The RVs derived from these models were used to disentangle the observed spectra and to determine a temperature for each component (see Sect. 4.1.1.3). The resulting temperatures and gravities were then used to choose the final pair of models, to compute the corresponding RVs and to derive the fundamental properties of the studied stars. The second procedure (further explained in Sect. 4.1.2.1) consisted in computing the RVs with several pairs of models. The pair of models providing velocities that best fit to a RV curve model was considered to be the optimum pair. In both cases, the obtained RVs were corrected to the heliocentric reference frame using standard IRAF routines.

Both procedures provide equivalent results, and the RVs computed with the first procedure (involving disentangling) were adopted for SB2A (Table 4.2). Of the nine observed spectra, only five are shown in Table 4.2. The remaining spectra (phases are shown in Fig. 4.2) were excluded during the W&D fit by sigma clipping (see Sect. 4.1.1.2). We found that, in general, rejected observations were obtained during eclipses or correspond to the spectrum having a shorter exposure time (observed in February 2005, Sect. 3.1.1). In both cases, TODCOR failed to identify a maximum of correlation in these spectra.

4.1.1.2 Mass and radius determination

The light and RV curves were modeled using the W&D code in order to derive the individual masses and radii of the components of each studied EB. Initial tests suggested that the light and RV curves should be modeled separately because of the very few RV measurements available and the possibility of inducing a bias in the mass ratio of the studied systems. Therefore, the light curve solutions of

Table 4.3. Fundamental properties of M31V J00443799+4129236 (SB2A) derived from the analysis with W&D.

System properties			
B magnitude at maximum light (B_{max})[a]		19.19±0.02	mag
V magnitude at maximum light (V_{max})[a]		19.27±0.02	mag
Period (P)		3.549694±0.000010	days
Time of minimum (t_{min})		2 452 204.421±0.003	HJD
Inclination (i)		89.3±1.8	deg
Systemic velocity (γ)		-173±4	km s^{-1}
Semi-major axis (a)		33.0±0.7	R$_\odot$
Mass ratio ($q = \mathcal{M}_S/\mathcal{M}_P$)		0.65±0.03	
Temperature ratio ($T_{eff,S}/T_{eff,P}$)		0.817±0.015	
Flux ratio in B ($F_{B,S}/F_{B,P}$)[a]		0.49±0.02	
Flux ratio in V ($F_{V,S}/F_{V,P}$)[a]		0.50±0.02	
Flux ratio in V_{DIRECT} ($F_{D,S}/F_{D,P}$)[a]		0.50±0.03	
Component properties	Primary		Secondary	
Radius (R)	13.1±0.3	R$_\odot$	11.3±0.3	R$_\odot$
Mass ($\mathcal{M}$)	23.1±1.3	M$_\odot$	15.0±1.1	M$_\odot$
Surface gravity (log g in cgs)	3.57±0.03		3.51±0.04	
Radial velocity semi-amplitude (K)[b]	185±6	km s^{-1}	285±6	km s^{-1}
Synchronized rotational velocity ($v_{sync}\sin i$)	187±4	km s^{-1}	161±4	km s^{-1}

[a] Out of eclipse average: $\Delta\phi = [0.14 - 0.36, 0.64 - 0.86]$
[b] Including non-Keplerian corrections

Sect. 2.4.1 were used as the initial values for the RV curve fits. The obtained results were then used to fit the light curves. Fitting was carried out iteratively until full consistency was achieved.

For each light curve fit, the procedure described in Sect. 2.4.1 was followed. In the case of RVs, the adjustable parameters were the orbital semi-major axis (a), the mass ratio (q), and the systemic velocity (γ). Convergence in the fits was reached rapidly, and tests from different starting points indicated the uniqueness of the solution. For each converging solution, a 3σ clipping was performed on both RV curves to eliminate observations having outlier RVs. The final rms (root mean square) residuals in the light curves are 0.013 mag in B, 0.013 mag in V, and 0.046 mag in the DIRECT V light curve. The residuals of the RVs are 5.2 and 4.6 km s^{-1} for the primary and secondary components, respectively.

The light and RV curves, with their respective fits superimposed are shown in Fig. 4.2. It is worth to remark that the O'Connell effect observed in the light curves identify this EB as semi-detached (with the secondary filling the Roche lobe, see Sect. 2.4.1). The resulting best-fitting elements are listed in Table 4.3. Two massive stars are observed, with masses (and radii) of $\mathcal{M}_P = 23.1 \pm 1.3$ M$_\odot$ ($R_P = 13.1 \pm 0.3$ R$_\odot$) and $\mathcal{M}_S = 15.0 \pm 1.1$ M$_\odot$ ($R_S = 11.3 \pm 0.3$ R$_\odot$), for the primary and the secondary components, respectively.

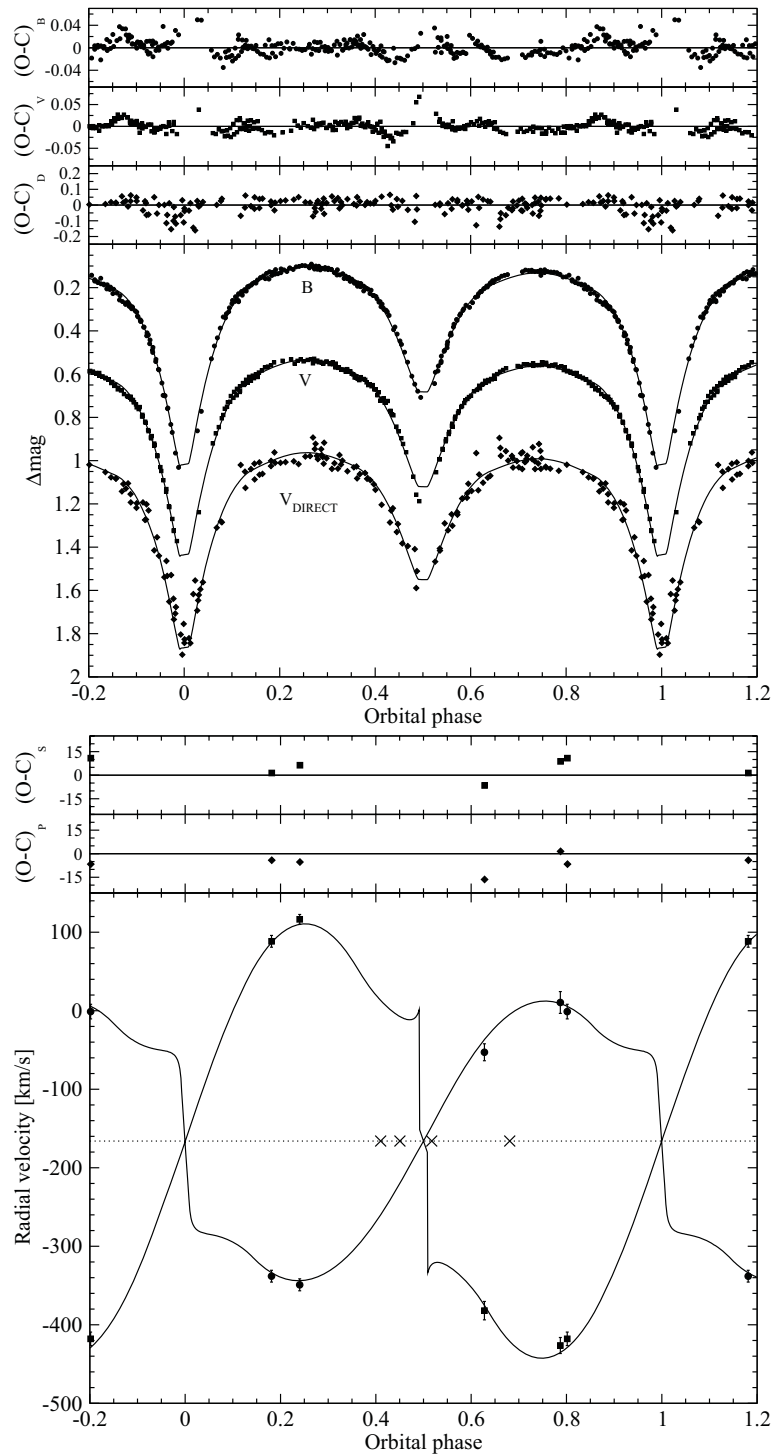One possible concern with light curves measured using DIA photometry is the

Figure 4.2. Observations for M31V J00443799+4129236 (SB2A) and corresponding W&D fits. **Top:** Light curve fits and corresponding residuals. **Bottom:** RV curve fits with RVs for the primary (circles) and secondary (squares) components with corresponding residuals. The phases of rejected RV observations are also indicated (crosses).

effect of an incorrect reference flux, which may cause a bias in the scale of the light curves (Michalska & Pigulski, 2005). Careful tests were carried out to ensure that this was not the case (Sect. 2.2.2). The excellent agreement between the fits to our DIA photometry and the fits to the DIRECT PSF photometry suggests that the flux zero-point is correct. In addition, we ran light-curve fits with a variable third-light contribution (l_3). A nonzero value (either positive or negative) of l_3 might indicate problems with the flux scale, but this did not occur, and the solutions converged to $l_3 \sim 0$. Such result has another interesting consequence of ruling out possible blends with unresolved companions. The absence of positive l_3 is not unexpected, since the light curves have the maximum possible depth ($i \sim 90$ deg) and preclude the existence of any additional light.

4.1.1.3   Temperature and distance determination

The last required ingredient to obtain a direct distance determination to M 31 is the temperature and absorption determination of SB2A. The photometric data available (i.e., B and V) are, by themselves, insufficient to determine the temperatures and reddening of the system. Therefore, two different approaches were attempted: modeling the spectra used for RV determinations and modeling the spectrophotometry.

Modeling of the optical spectra

The currently available stellar atmosphere models and line lists provide highly reliable synthetic spectra. These spectra, when compared with those observed, can provide accurate values of temperature, surface gravity, metallicity, etc. Therefore, we modeled the optical spectra with available stellar atmosphere models in order to derive the stellar temperature of the components in SB2A.

In EB systems, the spectra of both components are merged into a single spectrum and, therefore, the individual spectrum of each component has to be disentangled to accurately model the optical spectra. To perform this, we ran the KOREL program (Hadrava, 1995) by fixing all the parameters to the orbital solutions described in Sect 4.1.1.2. The resulting spectra are shown in Fig. 4.3.

Using a code developed by Edward L. Fitzpatrick at the Villanova University (Philadelphia), we then modeled the disentangled spectra using TLUSTY atmosphere models. Fits were constrained by the temperature ratio, surface gravities, and brightness ratio determined from the binary analysis. We solved for the constrained temperatures, a single metallicity for both components and individual values of $v_{\rm rot} \sin i$. The obtained values are listed in Table 4.4, and the best-fitting models are shown in Fig. 4.3, below each of the stellar spectra. Table 4.4 also lists values of M_V and $(B - V)_0$ for the components of the system. These values were
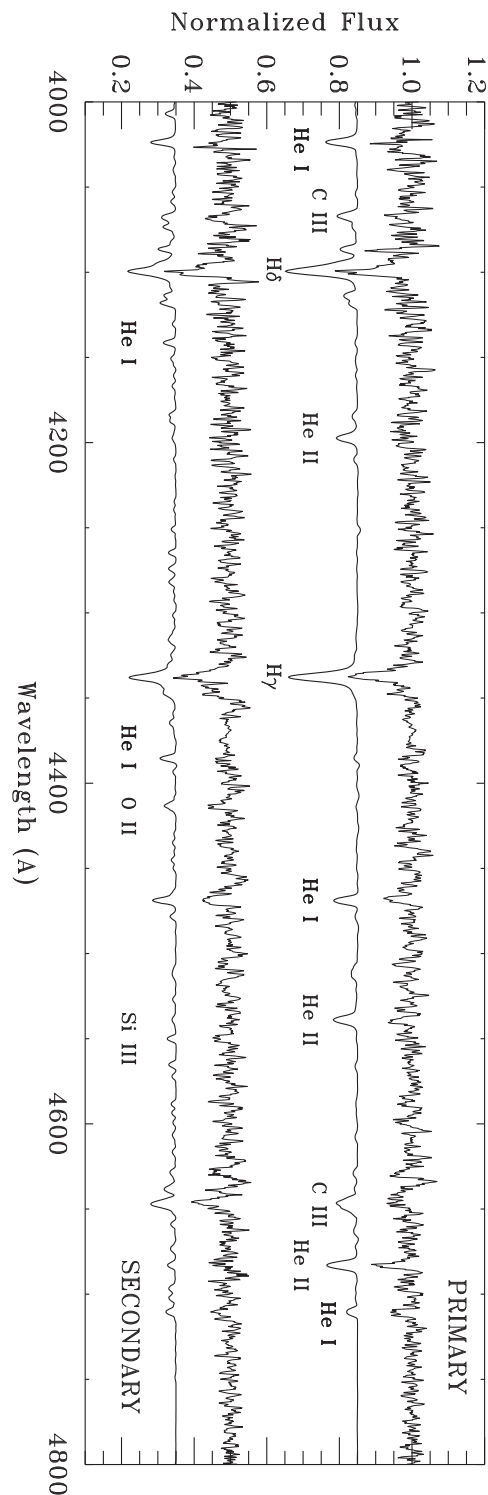
Figure 4.3. Comparison of the individual disentangled spectra for the EB M31V J00443799+4129236 (SB2A) with TLUSTY synthetic spectra. Some of the most intense spectral lines are labeled.

Table 4.4. Fundamental properties for M31V J00443799+4129236 (SB2A) and resulting distance determination, derived from the modeling of the optical spectra using TLUSTY atmosphere models and the values in Table 4.3.

System properties				
Metallicity ($[m/H]$)		-0.01±0.06		
Absolute V magnitude (M_V)		-5.77±0.06		mag
Color excess ($E(B-V)$)		0.19±0.03		mag
Line-of-sight absorption (A_V)		0.60±0.10		mag
Distance modulus ($(m-M)_0$)		24.44±0.12		mag
Component properties	Primary		Secondary	
Effective temperature (T_{eff})	33 900±500	K	27 700±500	K
Rotational velocity ($v_{\text{rot}} \sin i$)	230±10	km s^{-1}	145±8	km s^{-1}
Absolute V magnitude (M_V)	-5.29±0.07	mag	-4.66±0.07	mag
Intrinsic color ($(B-V)_0$)	-0.28±0.01	mag	-0.27±0.01	mag

computed by scaling the surface fluxes predicted by the TLUSTY models with the observed radii of the stars and performing synthetic photometry on the resultant energy distributions. The photometry was calibrated as described in Fitzpatrick & Massa (2005).

The 1σ uncertainties in the results of the spectral analysis were determined by a Monte Carlo technique. First, we created simulations of the spectra by combining our pair of best-fit models with 50 different random noise realizations, corresponding to S/N=40. For each simulated spectrum pair, we generated a simulated set of binary parameters (e.g., $T_{\text{eff},S}/T_{\text{eff},P}$) by combining the best-fit values with Gaussian noise, based on the 1σ uncertainties for each value. Finally, we fitted each pair of simulated spectra as described above, and adopted the standard deviations of the parameters among the 50 simulations as our uncertainties.

Once the fundamental properties are found, the calculation of the distance is straightforward, because the spectral analysis yields values for the absolute magnitudes of the components and also the combined M_V of the system (see Table 4.4). The distance modulus follows directly from the equation:

$$(m-M)_0 = V - M_V - A_V \tag{4.1}$$

To estimate the interstellar extinction (A_V), we compared the observed color ($B-V$) for the system with the intrinsic color ($(B-V)_0$) resulting from the spectral fit. Then we computed the total extinction from Eq. 1.10, with a total-to-selective extinction ratio of $\mathcal{R}_V = 3.1 \pm 0.3$ (Fitzpatrick & Massa, 2007). The overall procedure avoids the use of bolometric corrections and is self-consistent, as it employs the best-fitting model atmospheres (i.e., with the appropriate surface gravity and metallicity) to calculate the absolute M_V magnitudes and $(B-V)_0$ colors.

One basic point is a reliable estimation of the error budget. With the uncer-

tainty in M_V accounting for the full correlations of the intervening parameters, the rest of the quantities in the distance modulus equation are essentially uncorrelated. Thus, the contributions from the observed V magnitude (0.02 mag), M_V (0.06 mag), and A_V (0.10 mag) can be combined quadratically. From the parameters in Table 4.4 our calculation of the distance modulus to SB2A results in a value of $(m - M)_0 = 24.44 \pm 0.12$ mag or, equivalently, $d = 772 \pm 44$ kpc. This distance also corresponds to the center of M 31 itself, because the correction due to the location of the EB is negligible ($\sim 0.3\%$).

Spectrophotometry

We used the HST spectrophotometric measurements (reduced in Sect. 3.2) as an alternative approach to derive the temperature and absorption of the observed target. Following Fitzpatrick et al. (2003), the flux at a certain wavelength ($f_\lambda^\oplus$) of the observed EB is given by Eq. (1.13). The surface fluxes were obtained from TLUSTY atmosphere models and the normalized extinction curve was modeled as in Fitzpatrick & Massa (2007).

Some tests were performed in order to assess the capability of the obtained data to provide accurate temperature and extinction parameters. The results revealed that errors in the data were too large to obtain an accurate determination of the fitted parameters. In addition, the contamination of nearby stars in some of the observed spectra prevented from an accurate spectrophotometric modeling. Therefore, we decided to use the spectrophotometric data to check the accuracy of the temperature determinations resulting from the spectral fitting (described above) and, at the same time, to validate the procedure used.

All the parameters required to model the spectral energy distribution were fixed to the values resulting from the spectroscopic and photometric analysis. In order to introduce the effect of absorption, the mean galactic interstellar extinction curve was used (Fitzpatrick & Massa, 2007). As it is shown in Fig. 4.4, the model is compatible with the observations (that have errors in the range of 10–20%), but some systematics (of the order of 1σ) can be seen in the ultraviolet region (125–160 nm and around 200 nm) and in the infrared (600-1000 nm). On the one hand, some tests performed at the Villanova University with spectrophotometric standards reveal that the HRC/G800L calibration coefficients tend to provide standard fluxes that are too low, introducing the systematics in the infrared. When using a new set of coefficients (provided by a new recalibration with spectrophotometric standards) the observed systematics are corrected (as shown in the bottom panel of Fig. 4.4). On the other hand, the mean galactic extinction curve is affected by large uncertainties ($\sim 10\%$) in the ultraviolet part of the spectrum. Large differences in the extinction curve, depending on the line-of-sight, are the underlying reason for these uncertainties. Correspondingly, the modeled spectral energy distribution is affected by the same uncertainties, resulting in a systematic offset be-
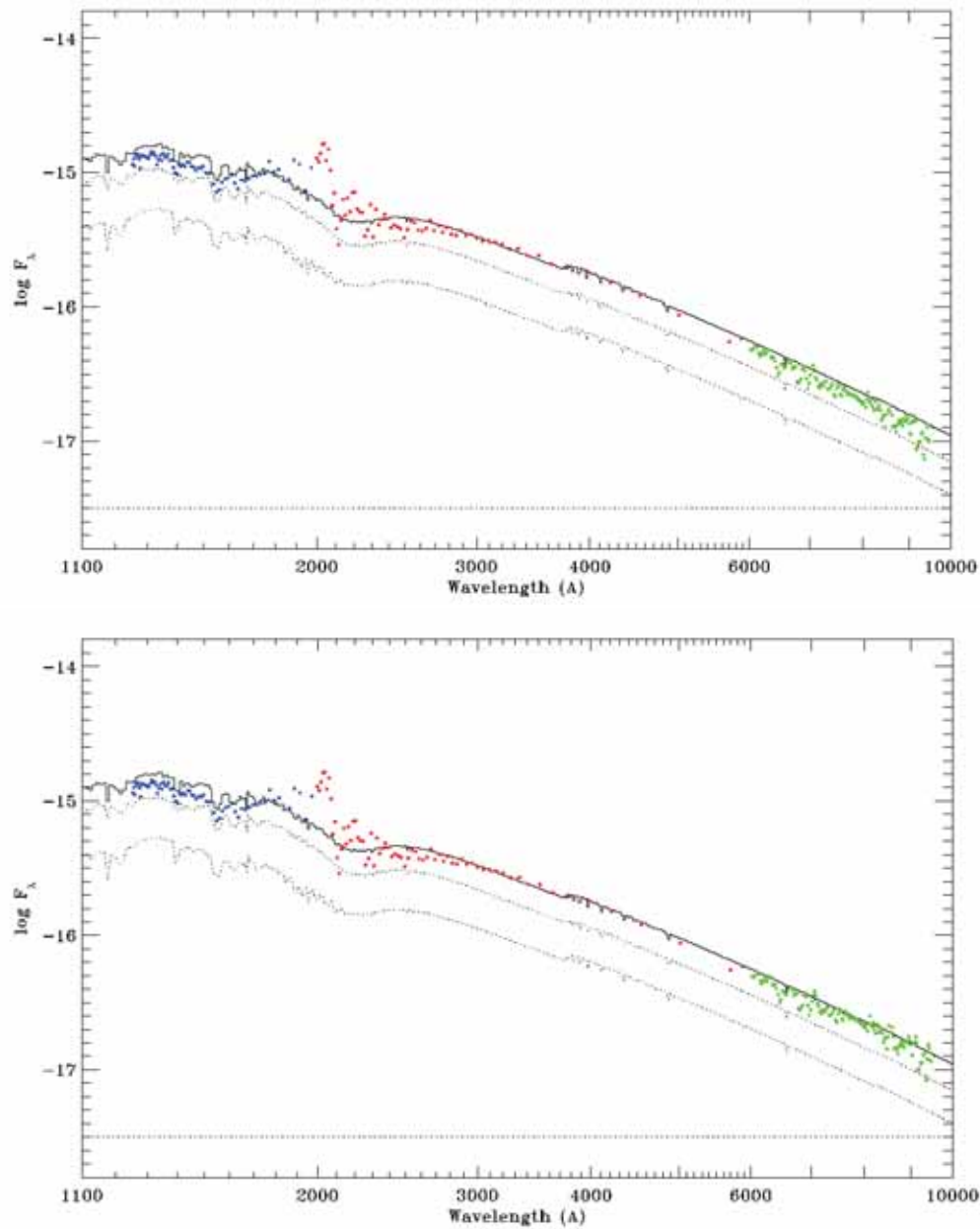
Figure 4.4. Spectral energy distribution for M31V J00443799+4129236 (SB2A). Dots correspond to the observations with the three ACS grisms used. Dotted lines represent the spectral energy distribution of each component, modeled according to the solutions derived from the spectroscopic and photometric analysis. The solid line is the combination of both components. **Top:** Calibrated values resulting from the implementation of the coefficients in the standard ACS reduction pipeline. **Bottom:** Calibrated values resulting from the implementation of a new set of coefficients provided by a new recalibration with spectrophotometric standards.

tween 110 and 160 nm. Finally, as shown in Sect 3.2.2.2, the large offset around
200 nm cannot be considered significant because of the large errors introduced
by a contaminating star in this region. Therefore, although some well understood
systematics ($\sim 1\sigma$) can be observed in the modeled spectrophotometry, the ob-
tained spectrophotometry can be considered to be compatible with the parameters
derived from the spectroscopic analysis and provides an independent confirmation
(within the relatively large uncertainties) of the fundamental properties of SB2A
(Table 4.3 and Table 4.4).

4.1.1.4 Comparison with stellar evolutionary models

The final step towards the characterization of SB2A is the comparison of the de-
rived physical properties with stellar evolutionary models. The comparison has
been mainly performed with the Geneva models of Lejeune & Schaerer (2001),
considering solar metallicity (according to the metallicity in Table 4.4). Other
models have been considered (Claret, 2004) without any major variations on the
derived conclusions. It is important to emphasize that the evolutionary tracks are
build for isolated stars. In close binary systems, the evolution of both stars can
be largely modified, with respect to their isolated evolutionary tracks, when one
of the components fills the Roche lobe and mass transfer takes place (see, e.g.,
Vanbeveren, 1993).

In order to take into account the effects of mass loss (due to stellar wind), the
mass of each component at the Zero-Age Main Sequence (ZAMS) was determined
by fitting different evolutionary tracks in the mass–radius diagram (Fig. 4.5, top).
The fitted tracks reveal that a 23.9 $M_\odot$ isolated star (i.e., with no mass transfer)
would have lost around 0.8 $M_\odot$ (comparable to the obtained error in mass) at the
current evolutionary stage. Therefore, mass loss is an important effect that has to
be considered when analyzing the evolutionary tracks of massive stars.

Once the evolutionary tracks are adopted, the Hertzsprung-Russell (hereafter
H-R) diagram can be studied (Fig. 4.5, bottom). The resulting locations of the
observed components reveal that both stars are overluminous for their masses. In
addition, the secondary component seems to be more evolved than the primary.
These results are in agreement with results obtained in other post-mass trans-
fer semi-detached systems (e.g., Fitzpatrick et al., 2003). In these systems, the
originally more massive component (currently the secondary) evolves beyond the
Roche lobe and some fraction of its mass is transferred to the companion star.
The mass transfer continues nowadays, when the mass-accreting component has
become the currently most massive component.

The proposed scenario is in agreement with the fact that the primary compo-
nent rotates faster than synchronization (see Table 4.3 and Table 4.4), since the
accreting mass also implies a transfer of angular momentum from the secondary
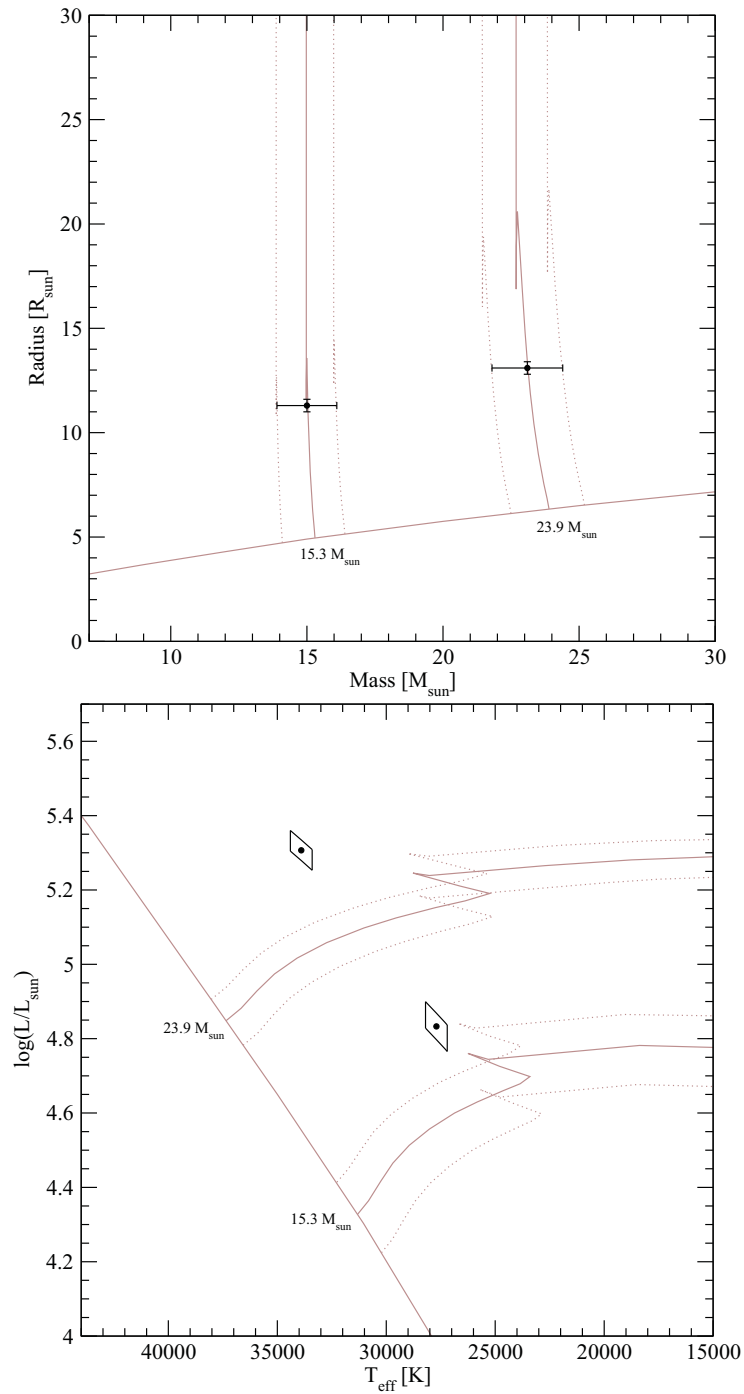(which is tidally locked, as can be assumed from the rotational velocities and 2σ

Figure 4.5. Comparison of stellar evolutionary models with derived physical properties of M31V J00443799+4129236 (SB2A). Gray solid lines correspond to the ZAMS and the evolutionary tracks (initial masses are labeled). Gray dotted lines denote the uncertainties in the derived masses. **Top:** Mass–radius diagram. **Bottom:** H-R diagram. The skewed rectangular boxes correspond to 1σ error loci.

error bars) to the primary. In other observed systems, the primary component is usually in better agreement with the corresponding evolutionary track. However, the mass transfer in SB2A seems to be really intense, with a bright hot spot that is synchronized with the rotational period of the system (as observed in the light curve). Since the primary component rotates ∼ 25% faster than synchronization, the material from the secondary component will impact the surface of the primary at different points. Therefore, the impacting material, combined with the proximity of both components, could increase the overall temperature (and luminosity) of the primary component.

4.1.2   M31V J00443610+4129194 (SB2B)

4.1.2.1   Radial velocities

The determination of RVs was performed, as in the case of SB2A (Sect. 4.1.1.1), with TODCOR and the ATLAS9 and TLUSTY synthetic models. In this case, the best pair of synthetic spectra was determined with a different iterative approach. As a first step, the preliminary W&D fit (Sect. 2.4.1) was used to define an initial list with pairs of models having a temperature ratio, gravity ratio and rotational velocities compatible with the W&D parameters. All the model pairs in the initial list were then used to determine RVs and a simple RV curve model was fitted to the obtained values. The free parameters in the fit were the semi-major axis (a), the systemic velocity (γ) and the mass ratio (q), whereas the period and reference time was fixed from the W&D solution. From all the derived solutions, the models having a lower dispersion around the fitted RV curve were selected and all the neighboring models in the space of parameters were also attempted. The process was repeated until the local minimum was found, (i.e., none of the neighboring models has a scatter lower than the selected pair of models).

Since the resulting RVs depend, to some extent, on the W&D fit, the obtained values were used to find a new solution with the W&D (Sect. 4.1.2.2). The resulting W&D solution was then used to determine new RVs. The process was repeated until the pair of synthetic models providing the best fit was the same in two iterations. The final solution shown in Table 4.5 contains all the RVs (corrected to the heliocentric reference frame) that remained after the W&D fit (with 3σ clipping). Rejected observations shown in Fig. 4.6 were obtained during eclipses (one of them correspond to the spectrum of February 2005 with a shorter exposure time).

The rejected observation close to phase 0.9 cannot be explained neither by the proximity to the nodes (since other observations are obtained at larger phases) nor by a lower S/N of the observed spectrum. Therefore, additional tests were performed. They revealed that the rejected observation could be recovered with different pairs of templates at the cost of losing other spectra close to the nodes and a larger dispersion of the fit. The obtained solutions had systemic velocities

Table 4.5. Radial velocity determinations for the EB M31V J00443610+4129194 (SB2B).

Time	Phase	Primary	Secondary
[HJD]		[km s^{-1}]	[km s^{-1}]
2 453 316.931	0.2719	-370.1±8.2	143.5±30.3
2 453 321.820	0.6586	14.3±13.9	-414.1±25.5
2 453 321.872	0.6836	57.3±13.5	-448.2±24.8
2 453 319.879	0.7111	30.6±9.9	-455.5±17.4
2 453 260.910	0.9265	-69.7±18.1	-309.2±19.4
2 453 295.776	0.9456	-58.1±24.2	-271.7±22.9

and semi-amplitudes in perfect agreement with the solution presented here. In addition, solutions with different W&D fits converged to the same pair of templates. The final reason for the incorrect RV determinations was found to be a casual correlation of the spectrum of the secondary with noise, which introduces a false correlation peak and biased RVs for this particular observation.

4.1.2.2 Mass and radius determination

The mass and radius determination was performed following the fitting procedure described for SB2A in Sect. 4.1.1.2. A configuration where the primary (instead of the secondary) fills the Roche lobe was used in this case. Both semi-detached configurations (with either the primary or the secondary filling the Roche lobe) provide fits with the same residuals. Therefore, the final configuration was adopted after the temperature determination analysis (Sect. 4.1.2.3). The spectra resulting from the disentangling indicate that the secondary is much fainter than the primary, whereas supposing that the secondary fills the Roche lobe provides a flux ratio of $F_{V,S}/F_{V,P} = 0.85$.

In order to ensure the viability of the adopted scenario, and to rule out any other possible configurations, additional fits supposing a detached configuration were performed. The resulting parameters revealed that, depending on the initial value of the surface potential of the secondary component, either the primary or the secondary tended to fill their respective Roche lobes.

With the adopted configuration, the final rms residuals are 0.014 mag in B, 0.015 mag in V, and 0.047 mag in the DIRECT V light curve. The residuals of the RVs are 13 and 6 km s^{-1} for the primary and secondary components, respectively. The light and RV curves, with their respective fits superimposed, are shown in Fig. 4.6. The resulting best-fitting elements listed in Table 4.6 reveal two components with masses very similar to those of SB2A, but smaller radii. The resulting masses (radii) are $\mathcal{M}_P = 21.7 \pm 1.7$ M$_\odot$ ($R_P = 9.2 \pm 0.2$ R$_\odot$) and $\mathcal{M}_S = 15.4 \pm 1.2$ M$_\odot$ ($R_S = 5.6 \pm 0.4$ R$_\odot$).
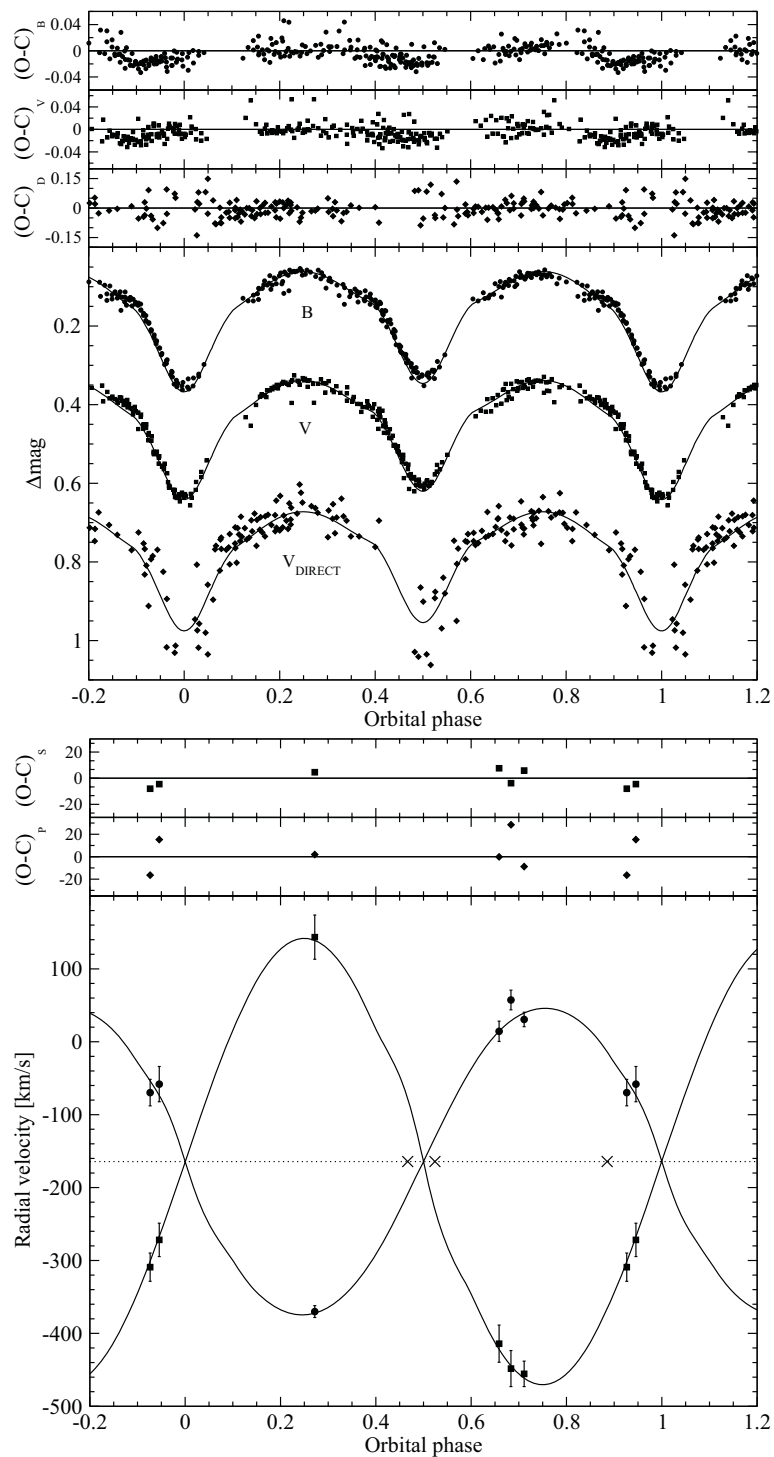
Figure 4.6. Observations for M31V J00443610+4129194 (SB2B) and corresponding W&D fits. **Top:** Light curve fits and corresponding residuals. **Bottom:** RV curve fits with RVs for the primary (circles) and secondary (squares) components with corresponding residuals. The phases of rejected RV observations are also indicated (crosses).

Table 4.6. Fundamental properties of M31V J00443610+4129194 (SB2B) derived from the analysis with W&D.

System properties		
B magnitude at maximum light $(B_{\max})^a$	19.832±0.013	mag
V magnitude at maximum light $(V_{\max})^a$	19.948±0.015	mag
Period (P)	2.048644±0.000007	days
Time of minimum $(t_{\min})$	2 452 908.694±0.004	HJD
Inclination (i)	69.9±1.6	deg
Systemic velocity (γ)	-164±5	km s^{-1}
Semi-major axis (a)	22.6±0.5	R$_{\odot}$
Mass ratio $(q = \mathcal{M}_S/\mathcal{M}_P)$	0.71±0.04	
Temperature ratio $(T_{\text{eff},S}/T_{\text{eff},P})$	0.897±0.019	
Flux ratio in B $(F_{B,S}/F_{B,P})^a$	0.33±0.03	
Flux ratio in V $(F_{V,S}/F_{V,P})^a$	0.33±0.03	
Flux ratio in V_{DIRECT} $(F_{D,S}/F_{D,P})^a$	0.33±0.05	

Component properties	Primary		Secondary	
Radius (R)	9.2±0.2	R$_{\odot}$	5.6±0.4	R$_{\odot}$
Mass $(\mathcal{M})$	21.7±1.7	M$_{\odot}$	15.4±1.2	M$_{\odot}$
Surface gravity (log g in cgs)	3.85±0.02		4.12±0.05	
Radial velocity semi-amplitude $(K)^b$	210±9	km s^{-1}	306±11	km s^{-1}
Synchronized rotational velocity $(v_{\text{sync}} \sin i)$	213±6	km s^{-1}	131±8	km s^{-1}

^{a} Out of eclipse average: $\Delta\phi = [0.20 - 0.30, 0.70 - 0.80]$
^{b} Including non-Keplerian corrections

Following the reasoning in Sect. 4.1.1.2, several light-curve fits were performed with a variable third-light contribution (l_3). Again, the excellent agreement between the DIRECT light curve to our photometry and the convergence of the fits to $l_3 \sim 0$, ensures that the flux zero-point is correct and rules out any possible blends with unresolved companions.

4.1.2.3 Temperature and distance determination

The only data available for SB2B to perform a temperature determination are the GMOS spectra. Therefore, as in Sect. 4.1.1.3, we determined the temperature of the components by modeling the disentangled spectra from the KOREL program. The parameters obtained in Sect. 4.1.2.2 were used for performing the disentangling. It is important to emphasize that the RV curve depends only slightly on the configuration adopted. Therefore, the disentangled spectra (Fig. 4.7) can be considered the same for the case when the primary or the secondary fills the Roche lobe.

The disentangling provided an spectrum for the secondary component mainly dominated by noise. This is not surprising considering the derived flux ratio ($F_{V,S}/F_{V,P} = 0.33$) and the S/N of the observed spectra, resulting in a spectrum
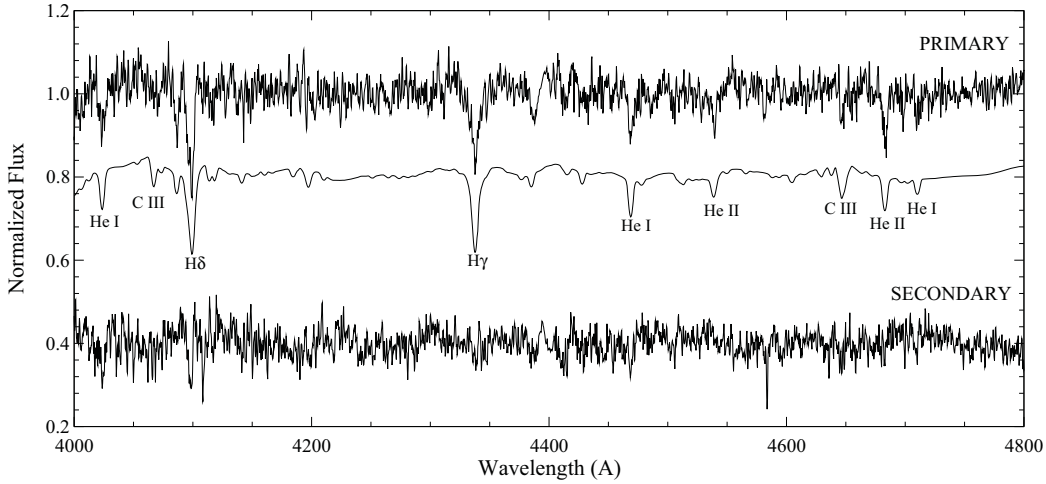
Figure 4.7. Comparison of the individual disentangled spectrum for the primary component of M31V J00443610+4129194 (SB2B, above) with the TLUSTY synthetic spectrum (middle). The bottom spectrum shows the disentangled spectrum of the secondary component.

for the secondary with a S/N~10. In a system where both components are equally bright, each component has a similar contribution to the combined spectrum, resulting in disentangled spectra that have a similar S/N. Therefore, the disentangled spectra indicate that the secondary component is clearly fainter than the primary component. As previously mentioned (Sect. 4.1.2.2), supposing that the secondary fills the Roche lobe results in a flux ratio $F_{V,S}/F_{V,P} = 0.85$, which is clearly in contradiction with the results provided by the disentangling. Then, the scenario where the secondary fills the Roche lobe can be excluded, since a flux ratio of $F_{V,S}/F_{V,P} = 0.85$ should result in a spectrum with a S/N~25 for the secondary, similar to the best quality observed spectra.

Considering the low S/N of the secondary, the fitting procedure was restricted to the primary component. The temperature (T_{eff}), surface gravity ($\log g$) and rotational velocity ($v_{\text{rot}} \sin i$) were fitted considering TLUSTY templates with solar metallicity. The resulting values are listed in Table 4.7 together with the values of absolute luminosity (M_V) and intrinsic color ($(B - V)_0$). These values were computed by scaling the absolute magnitude in the models of Lejeune & Schaerer (2001) (for a given temperature and gravity) with the observed radii of the stars. When needed, the values resulting from the W&D fit were used (e.g., to determine the temperature of the secondary). This procedure is equivalent to the one used in Sect. 4.1.1.3, where instead of performing the synthetic photometry to obtain the surface fluxes (as in the case of SB2A), they were obtained from the models.

Finally, once the absolute magnitudes of the components are determined, the determination of the distance is straightforward (Sect. 4.1.1.3). The resulting distance modulus to SB2B is $(m - M)_0 = 24.30 \pm 0.11$ mag or, equivalently,

Table 4.7. Fundamental properties of M31V J00443610+4129194 (SB2B) and resulting distance determination, derived from the modeling of the optical spectrum of the primary component, using TLUSTY atmosphere models and the values in Table 4.6.

System properties				
Absolute V magnitude (M_V)		-4.90±0.08		mag
Color excess ($E(B-V)$)		0.18±0.02		mag
Line-of-sight absorption (A_V)		0.55±0.08		mag
Distance modulus (($m-M)_0$)		24.30±0.11		mag
Component properties	Primary		Secondary	
Effective temperature (T_{eff})	33 600±600	K	30 100±900	K
Surface gravity (log g in cgs)	3.86±0.12		—	
Rotational velocity ($v_{\text{rot}} \sin i$)	189±12	km s^{-1}	—	
Absolute V magnitude (M_V)	-4.59±0.07	mag	-3.38±0.12	mag
Intrinsic color (($B-V)_0$)	-0.295±0.002	mag	-0.286±0.004	mag

$d = 724 \pm 37$ kpc.

4.1.2.4 Comparison with stellar evolutionary models

In order to compare the derived properties of SB2B with stellar evolutionary models, the procedure described in Sect. 4.1.1.4 was followed. The location of the studied components on the H-R diagram (Fig. 4.8) reveals that both components agree with their predicted evolutionary tracks.

The derived properties seem characteristic of a detached system. However, as explained in Sect. 4.1.2.2, the W&D solutions supposing a detached configuration converge to solutions where either the primary or the secondary fill their respective Roche lobes. In addition, the disentangled spectra seem to favor the case where the primary is filling the Roche lobe, since it is much brighter than the secondary. All these observations can be explained supposing that SB2B is a pre-mass transfer EB system, where the primary component is *almost* filling its Roche lobe.

In a pre-mass transfer EB, both components are detached and basically follow the evolution of single stars. This explains why the observed properties agree with the evolutionary tracks, since each component has evolved without any major interaction with the other component. This could also explain why the most massive component can be assumed to be filling the Roche lobe. What is generally observed in semi-detached EBs is the Algol paradox, where the donor is the less massive component (as in the case of SB2A, described in Sect. 4.1.1.4). The reason of this phenomenon (Paczyński, 1971) is that, when the donor is more massive than the companion, the mass transfer is very rapid, taking place on a thermal time scale ($\sim 10^5$ yr). On the contrary, when the donor is less massive
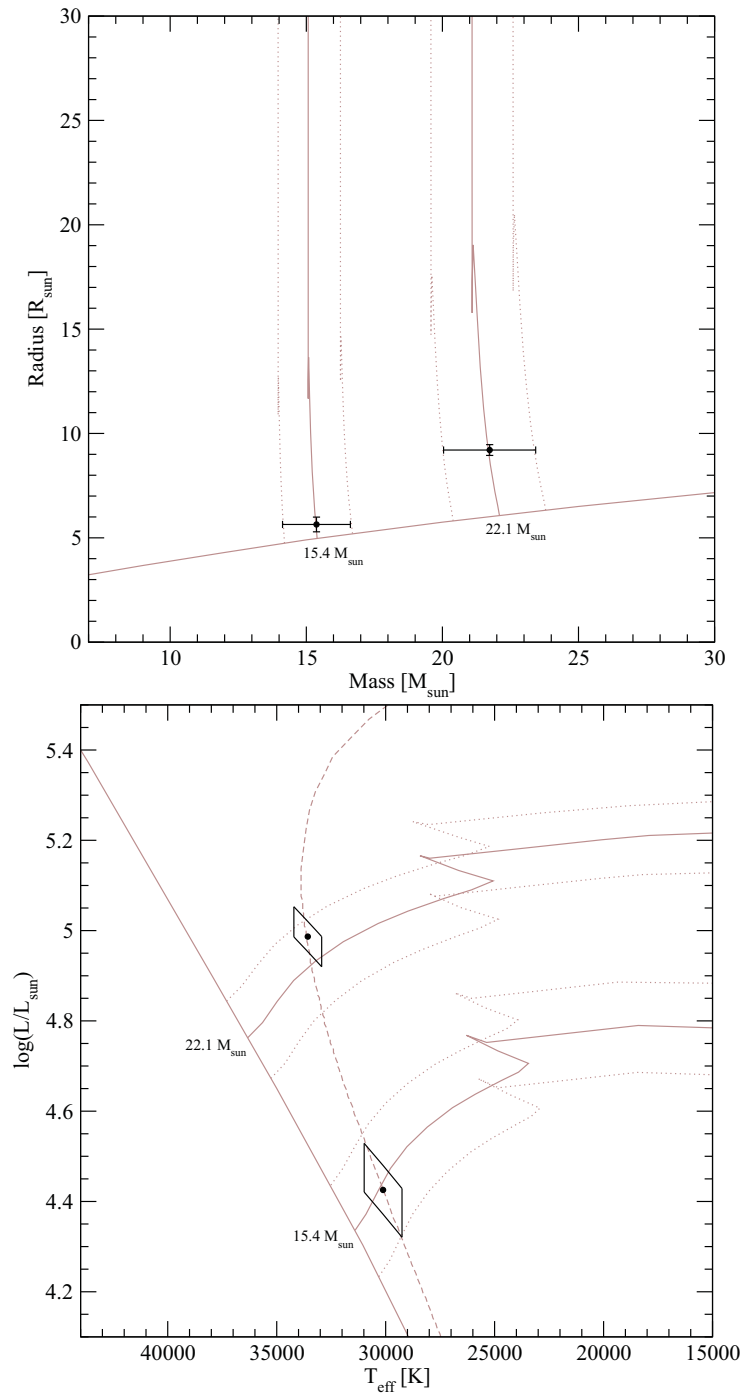
Figure 4.8. Comparison of stellar evolutionary models with derived physical properties of M31V J00443610+4129194 (SB2B). Gray solid lines correspond to the ZAMS and the evolutionary tracks (initial masses are labeled). The best fitting isochrone of 4.2 Myr is also shown (gray dashed line). Gray dotted lines denote the uncertainties in the derived masses. **Top:** Mass–radius diagram. **Bottom:** H-R diagram. The skewed rectangular boxes correspond to 1σ error loci.

than the companion, the mass transfer can last as long as the main-sequence life-time of the donor. The lack of any signature of intense mass transfer (such an O'Connell effect in the light curves), combined with the short timescale of the process, makes that a situation where the most massive component is filling the Roche lobe is unlikely. In addition, the time spent in a situation where a massive star (like the ones observed) can be almost filling the Roche lobe is somewhat longer than the thermal timescale (~ 0.5 Myr), making the situation more likely to be observed.

The close agreement of the observations with the theoretical models, apart from clarifying the evolutionary stage of SB2B, also allowed the fitting of an isochrone, resulting in an estimated coeval age of 4.2 ± 0.4 Myr.

4.1.3 M31V J00444528+4128000 (SB1)

4.1.3.1 Radial velocities

A close look at the acquired spectra of SB1 (the brightest EB in the variable star catalog) revealed no signs of features belonging to the secondary component. In addition, several attempts were performed to determine RVs (with TODCOR) assuming that SB1 has double lines, with no physically valid results. Therefore, SB1 was assumed to be a single-line EB.

The brightness of SB1 has made that the GMOS spectra have a relatively high S/N, allowing the use of algorithms to determine the RVs that are independent of synthetic templates. Therefore, a specific algorithm (called TIRAVEL, Zucker & Mazeh, 2006) was used to determine the RVs. The most important advantage of using TIRAVEL (with respect to cross-correlation algorithms) is that no assumption has to be made, either on the EB model nor on the atmosphere of the star. Radial velocities are determined from the relative displacement of the lines among the obtained spectra and, hence, no information on the absolute RVs is obtained. However, TIRAVEL is capable to provide a merged spectrum (with higher S/N) from all the observed spectra. The merged spectrum is analyzed in the temperature determination process (Sect. 4.1.3.2) and, as a by-product, its absolute RV is obtained. Since the merged spectrum has a null relative RV, the derived RV corresponds to the difference between the absolute RVs and the relative RVs provided by TIRAVEL.

It is worth mentioning that TIRAVEL can only use 2048 points of each spectrum. Therefore, the observed GMOS spectra were split into two parts (361.1–456.8 nm and 410.9–506.5 nm) and independent radial velocities were obtained (Table 4.8). Both RVs were averaged to obtain the RVs for the primary component (corrected to the heliocentric reference frame) shown in Table 4.8.

In order to estimate the uncertainties of the RVs provided by TIRAVEL, a

Table 4.8. Relative radial velocity determinations for M31V J00444528+4128000 (SB1). For each spectrum, two RVs were derived: one for the part with shorter wavelengths (361.1–456.8 nm, blue part) and one for the part with longer wavelength (410.9–506.5 nm, red part). The RVs of the primary component are the mean of both results.

Time [HJD]	Phase	Blue RVs km s^{-1}	Red RVs km s^{-1}	Primary [km s^{-1}]
2 453 316.931	0.1461	-70.1	-63.6	-66.9±4.4
2 453 260.910	0.2931	-72.3	-63.7	-68.0±4.3
2 453 295.776	0.3135	-84.5	-84.6	-84.6±4.4
2 453 319.879	0.4015	-44.6	-42.5	-43.6±4.4
2 453 262.874	0.4633	-5.3	-11.6	-8.4±4.5
2 453 413.734	0.5319	25.6	33.6	29.6±3.9
2 453 264.066	0.5665	79.4	62.4	70.9±4.5
2 453 321.820	0.5697	53.4	51.9	52.7±4.3
2 453 321.872	0.5741	57.7	57.6	57.6±4.5

program performing simple cross-correlation was applied to each one of the nine observed spectra. The cross-correlation technique requires a template. In this case, a TLUSTY spectrum with properties similar to those derived after the temperature determination (Sect. 4.1.3.2) was used as template. The uncertainties derived from the correlation were considered to be the uncertainties in the RVs of the primary component. As shown in Table 4.8, the derived uncertainties make the two independent RVs provided by TIRAVEL fully compatible. Finally, the RVs resulting from the correlation program also enabled an independent check on the RV determinations provided by TIRAVEL, confirming the obtained values within the error bars.

4.1.3.2   Temperature determination

As previously mentioned (Sect. 4.1.3.1), we used the combined spectrum provided by TIRAVEL to determine the temperature of the primary component. The combined spectrum was modeled using TLUSTY model atmospheres (Fig. 4.9). The good quality of the spectrum (S/N~70) allowed a complete characterization of the fundamental properties of the primary component (Table 4.9), including metallicity ($[m/H]$), microturbulent velocity (v_{micro}) and rotational velocity ($v_{rot} \sin i$). These quantities have a small effect on the final temperature and absolute magnitude of the modeled star, but provide additional information on the fundamental properties of the system. Of particular interest is the low surface gravity derived ($\log g = 2.57 \pm 0.03$ dex), indicating that the primary component of SB1 is evolved. This was expected, since the comparison of the spectrum with that of other blue supergiants (e.g, HD 38771, HD 152234) already classified this star as evolved.
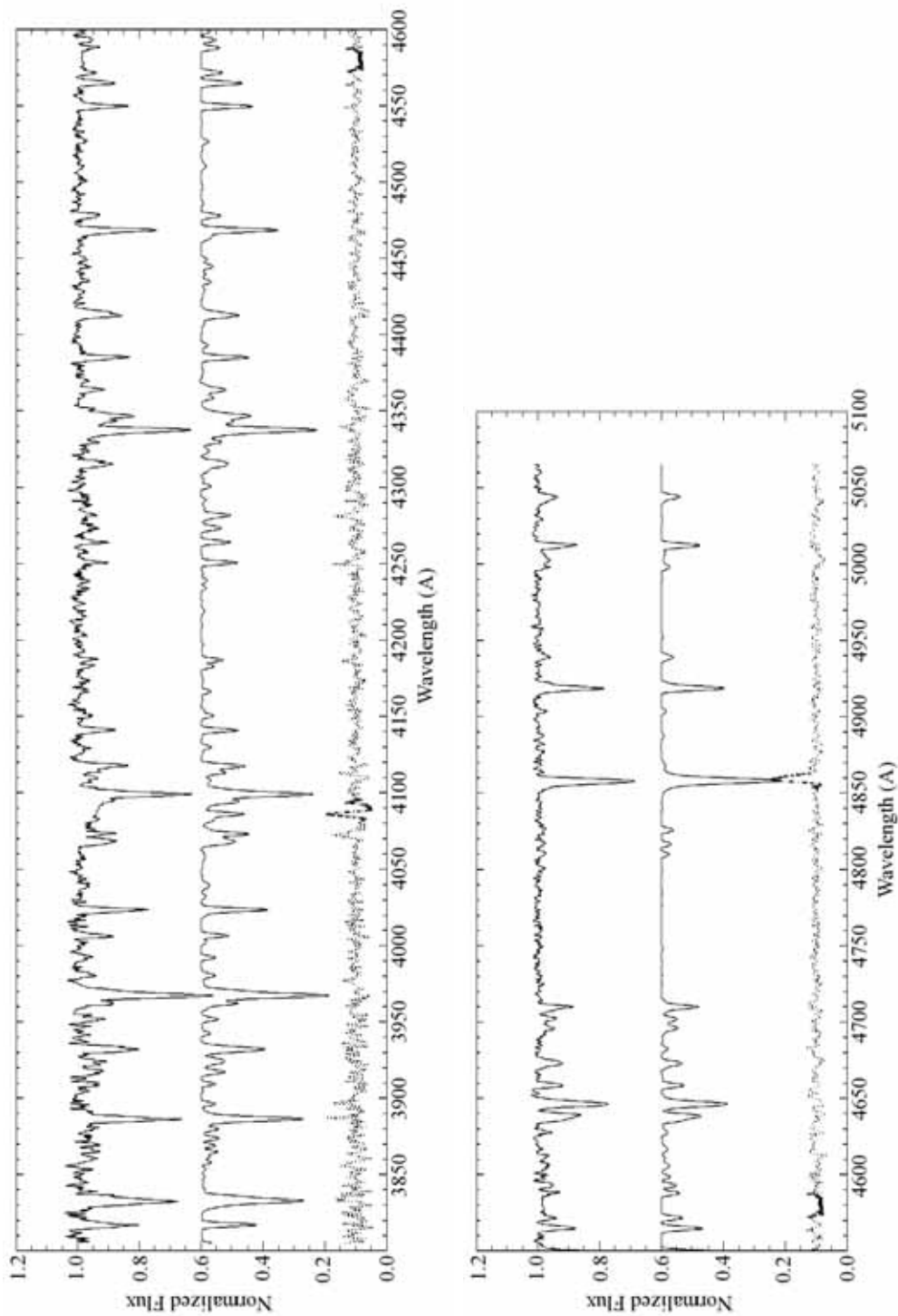
Figure 4.9. Comparison of the combined spectrum of the primary component of M31V J00444528+4128000 (SB1, up) with TLUSTY synthetic spectra (middle). The residuals of the fit are also shown (below, dotted line). Dark zones in the residuals (around 409 nm, 458 nm and 486 nm) show areas excluded from the fit.

Table 4.9. Parameters derived from the modeling of the merged spectrum for M31 V J00444528+4128000 (SB1). TLUSTY atmosphere models and the values in Table 4.10 were used.

System properties			
Merged spectrum RV		-205.2±1.8	km s^{-1}
Metallicity ($[m/H]$)		-0.24±0.06	
Absolute magnitude (M_V)		-6.6±0.2	mag
Color excess ($E(B-V)$)		0.29±0.05	mag
Absorption (A_V)		0.90±0.17	mag
Component properties	Primary	Secondary	
Effective temperature (T_{eff})	21 200±300 K	11 200±700 K	
Surface gravity ($\log g$ in cgs)	2.57±0.03	—	
Rotational velocity ($v_{\text{rot}} \sin i$)	127±3 km s^{-1}	—	
Microturbulent velocity (v_{micro})	24.9±1.5 km s^{-1}	—	
Absolute V magnitude (M_V)	-6.4±0.2 mag	-4.6±0.3 mag	
Intrinsic color (($B-V)_0$)	-0.232±0.002 mag	-0.096±0.031 mag	

Table 4.9 also lists values of M_V and $(B-V)_0$ for the system. The absolute magnitude of the primary component was derived after determining the absorption to primary component (Eq. 1.10) and correcting the observed V magnitude at maximum (Table 4.10) for the distance modulus of $(m-M)_0 = 24.44 \pm 0.12$ mag[3] (Table 4.4) and the flux ratio in V (Table 4.10). The intrinsic color was derived from the temperature and surface gravity, and using intrinsic colors tabulated in Lejeune & Schaerer (2001). The flux ratio in V passband and the temperature ratio (Table 4.10) were also used to determine the absolute luminosity of the secondary component. As in previous EBs, the reported uncertainties were obtained using the Monte Carlo technique with 20 different random noise realizations, corresponding to S/N=70.

4.1.3.3   Mass and radius determination

The mass and radius determination was performed following the fitting procedure described in Sect. 4.1.1.2. In this case, however, the lack of the signature of the secondary component (which is supposed to be filling the Roche lobe) in the spectra makes that the semi-major axis or the mass ratio have to be fixed in the W&D fit (Eq. 1.3). In our case, the relative radius of the primary can be obtained from the light curve fit and the absolute radius can be obtained from the absolute magnitude, since the effective temperature is known (Sect. 4.1.3.2). Therefore, the

---

[3]The distance modulus for SB2A is used instead of the mean value of Sect. 4.2 because the distance determination to SB2B was not available when this work was performed. In any case, the similarity of both results, well within the error bars, and the fact that SB2A has a temperature determination for both components, makes that the distance to SB2A can be considered highly accurate and capable, by itself, to fulfill the requirements of this analysis.

Table 4.10. Fundamental properties of M31V J00444528+4128000 (SB1) derived from the analysis with W&D.

System properties			
B magnitude at maximum light $(B_{\max})^a$		18.80 ± 0.02	mag
V magnitude at maximum light $(V_{\max})^a$		18.73 ± 0.03	mag
Period (P)		11.5435 ± 0.0004	days
Time of minimum $(t_{\min})$		$2\,451\,814.55 \pm 0.03$	HJD
Inclination (i)		66 ± 2	deg
Systemic velocity (γ)		192 ± 4	km s^{-1}
Semi-major axis (a)		74 ± 5	R$_\odot$
Mass ratio $(q = \mathcal{M}_S/\mathcal{M}_P)$		0.51 ± 0.09	
Temperature ratio $(T_{\mathrm{eff},S}/T_{\mathrm{eff},P})$		0.53 ± 0.03	
Flux ratio in B $(F_{B,S}/F_{B,P})^a$		0.17 ± 0.02	
Flux ratio in V $(F_{V,S}/F_{V,P})^a$		0.19 ± 0.03	
Flux ratio in V_{DIRECT} $(F_{D,S}/F_{D,P})^a$		0.19 ± 0.03	
Component properties	Primary		Secondary	
Radius (R)	33 ± 3	R$_\odot$	23 ± 2	R$_\odot$
Mass $(\mathcal{M})$	26 ± 7	M$_\odot$	14 ± 2	M$_\odot$
Surface gravity $(\log g$ in cgs$)$	2.82 ± 0.05		2.84 ± 0.04	
Radial velocity semi-amplitude $(K)^b$	95 ± 7	km s^{-1}	184 ± 23	km s^{-1}
Synchronized rotational velocity $(v_{\mathrm{sync}} \sin i)$	132 ± 13	km s^{-1}	92 ± 5	km s^{-1}

^{a} Out of eclipse average: $\Delta\phi = [0.20 - 0.32, 0.68 - 0.80]$
^{b} Including non-Keplerian corrections

semi-major axis was fixed (after several iterations) so that the absolute radius of the primary was consistent with the value derived from the temperature determination process. The error in the radius determination was propagated to the derived quantities by performing several fits with the W&D using semi-major axis values in the range of the computed errors. The final rms residuals are 0.02 mag for the B light curve, 0.03 mag for both V light curves and 8 km s^{-1} for the RV curve. The light and RV curves, with their respective fits superimposed, are shown in Fig. 4.10.

The relatively large scatter in the resulting light curve fits cannot be explained entirely by the statistical error of the observations. In fact, the different clumps observed in the residuals (Fig. 4.10) correspond to observations taken during the same night, indicating that one of the components (or both) is intrinsically variable. Errors reported by W&D suppose that the dispersion of the fit is entirely due to random noise. Therefore, the variability observed in the light curves makes that the derived errors are likely not representative of the uncertainties in the derived parameters, even considering that a conservative value was adopted.

The resulting best fit elements for both components listed in Table 4.10 reveal two components with masses similar to those of SB2A and SB2B ($\mathcal{M}_P = 26 \pm 7$ M$_\odot$ and $\mathcal{M}_S = 14 \pm 2$ M$_\odot$). However, the derived radii are much larger ($R = 33 \pm 3$ R$_\odot$ and $R = 23 \pm 3$ R$_\odot$), which suggests that the components are evolved. In fact,
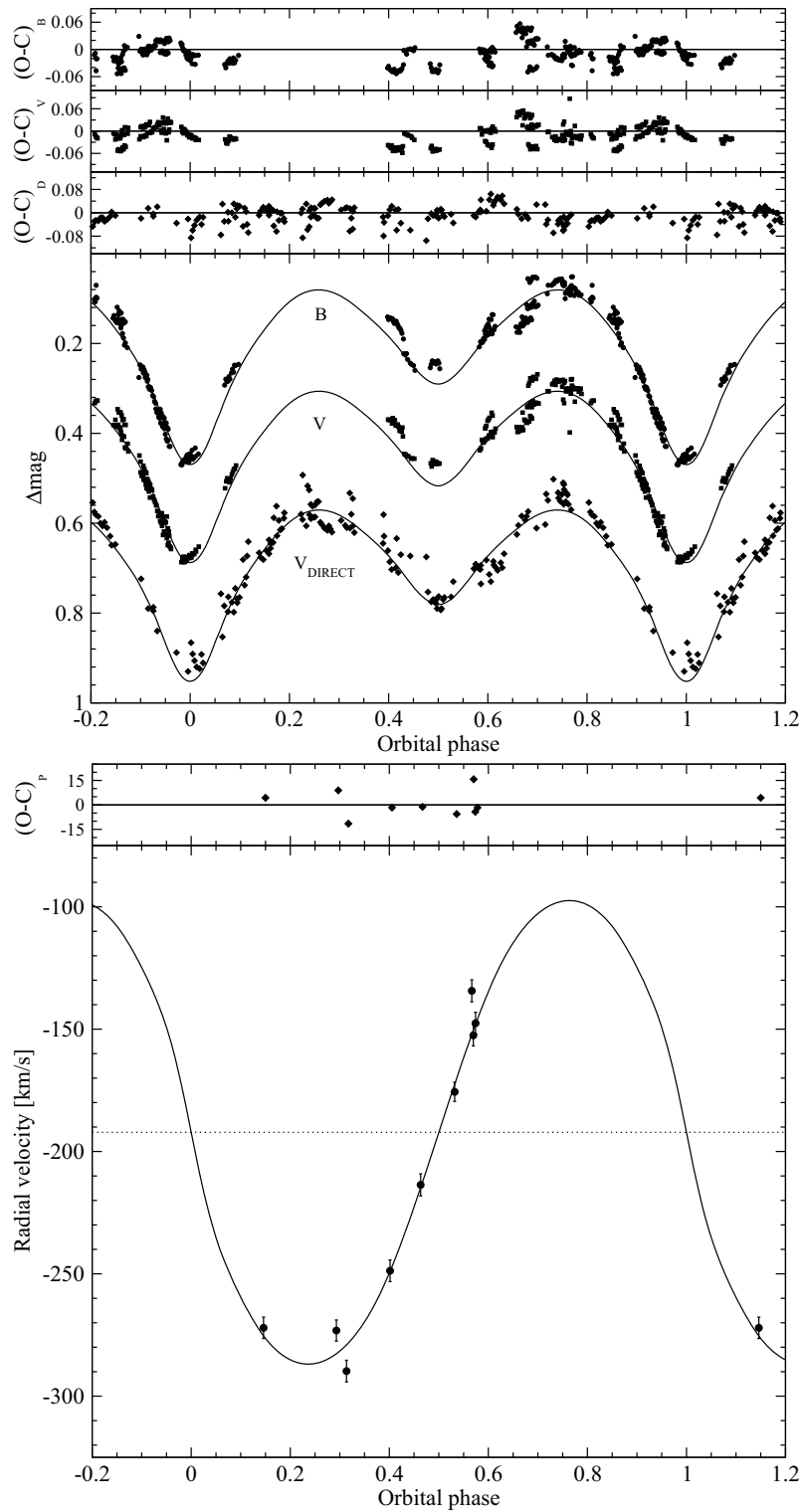
Figure 4.10. Observations for M31 V J00444528+4128000 (SB1) and corresponding W&D fit. **Top:** Light curve fits and corresponding residuals. **Bottom:** RV curve fit with corresponding residuals.

the primary is almost filling the Roche lobe and, therefore, both components are almost in contact.

4.1.3.4 Comparison with stellar evolutionary models

As done in previous cases, the derived properties of M31V J00444528+4128000 (SB1) were compared with the stellar evolutionary models of Lejeune & Schaerer (2001). Again, the mass-radius diagram was used to consider the effect of mass loss and to derive evolutionary tracks with solar metallicity (Fig. 4.11).

The H-R diagram reveals that the primary component is at a phase of core helium burning. The derived evolutionary status is in agreement with the observed spectrum, which is typical of stars with luminosity class between Ia and Ib (Sect. 4.1.3.2). The supergiant nature of the primary component could well explain the observed scatter of $\sim$ 0.02 mag in the residuals of the W&D fit (Sect. 4.1.3.3), since some of these stars are known to be variable (e.g., HD 86606, HD 148688, HD 169454). The derived radius, when compared with the rotational velocity (Table 4.9), indicates that the primary component rotational period is synchronized with the orbital period, which is expected since both components are almost in contact. The gravity value of $\log g = 2.82 \pm 0.05$ obtained with W&D for the primary component, is not consistent with the value of $\log g = 2.65 \pm 0.03$ derived from the spectroscopic fit (where the value of $\log g = 2.57 \pm 0.03$ was corrected from the centrifugal force, Fitzpatrick & Massa, 2005). However, there are two possible causes that could explain the difference between the observed and the modeled surface gravity. In first place, both components of SB1 are highly distorted by the presence of the nearby companion, with radius variations along their surfaces on the order of 10% (3 $R_\odot$ for the primary component) that greatly modify the surface gravity. Secondly, radiation pressure is known to have a non-negligible contribution in post-core-hydrogen-burning stars (see, e.g., Lamers & Fitzpatrick, 1988), making that the observed surface gravity of these stars is lower than expected for a given mass and radius. Therefore, all the derived properties identify this component as the first extragalactic blue supergiant with a dynamical determination of its mass and radius.

The secondary component is clearly underluminous for its mass. The low luminosity value cannot be explained by a circumstellar disk, since the secondary is filling its Roche lobe. In addition, supposing that the primary (instead of the secondary) fills the Roche lobe in the W&D fit results in parameters that are almost identical to the values presented in Table 4.10, excluding the possibility of a circumstellar disk. The disagreement with the evolutionary track cannot be explained by supposing that the luminosity of the secondary is in error, since a brighter secondary (with $F_{V,S}/F_{V,P} > 0.2$) would make that spectral lines were visible in the observed spectrum. Therefore, the most likely reason for the observed discrepancy is in the mass determination of the secondary. The mass of the secondary
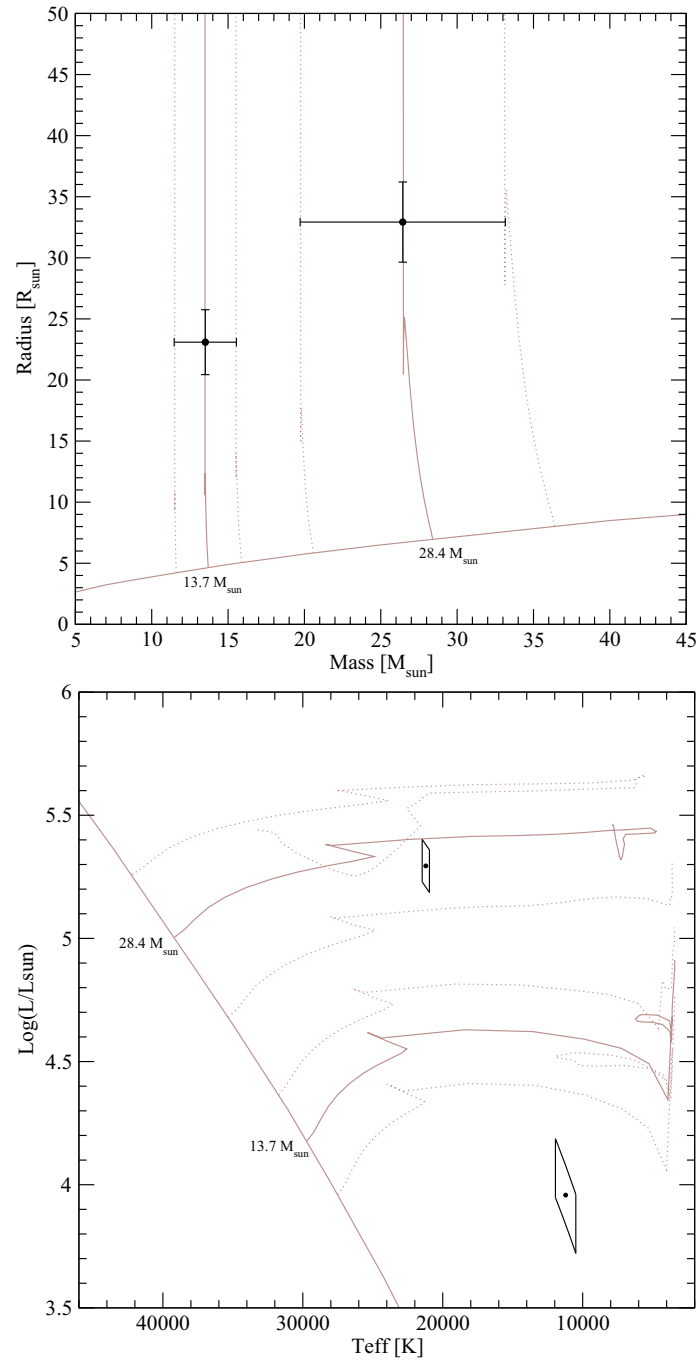
Figure 4.11. Comparison of stellar evolutionary models with derived physical properties of M31V J00444528+4128000 (SB1). Gray solid lines correspond to the ZAMS and the evolutionary tracks (initial masses are labeled). Gray dotted lines denote the uncertainties in the derived masses. **Top:** Mass–radius diagram. **Bottom:** H-R diagram. The skewed rectangular boxes correspond to 1σ error loci. Any possible systematic errors introduced by the variability observed in the light curves are not included.

is entirely derived from the mass ratio, which depends on the assumed value of the semi-major axis. In order to allow a different value of the semi-major axis without changing the absolute radius of the primary component (derived independently from the W&D fit), the relative radius of the primary should compensate the difference in the semi-major axis. In this sense, the relative radius of the primary could have some systematic error, since it is determined from light curves that present some variability. A systematic error (~ 10%) on the *relative* radius of the primary could explain the observed discrepancy between the evolutionary tracks and the derived properties of the secondary component. A light curve obtained during a single period (to reduce the effects of variability) could be worthy to clarify the real cause of the observed discrepancy. However, the identification of the lines of the secondary component would be definitive, since they would enable the determination of the mass ratio. Unfortunately, a telescope larger than Gemini-North is required.

4.1.4   M31V J00442326+4127082 (SB3)

4.1.4.1   Radial velocities

Three independent results support the idea that SB3 is a triple-line EB. First, the large third light contribution ($l_3 = 0.33$) derived from the preliminary light-curve analysis (Table 2.3). Second, the spectral lines are severely blended, even at quadratures (Fig. 4.12). And, finally, the RVs obtained supposing a double-line EB provide unphysical results or large residuals. Therefore, we decided to run a three-dimensional cross-correlation algorithm (TRIMOR) to determine the RVs of the three components.

TRIMOR (developed at the School of Physics of Astronomy of the Tel Aviv University in Israel) is a generalization of the TODCOR code used for the double-line EBs, prepared to perform three-dimensional cross-correlations for single-order or multi-order spectra. Therefore, the RV determination was performed following a similar procedure to that used for SB2B (Sect. 4.1.2.1). The main dif-

Table 4.11.   Radial velocity determinations for M31V J00442326+4127082 (SB3).

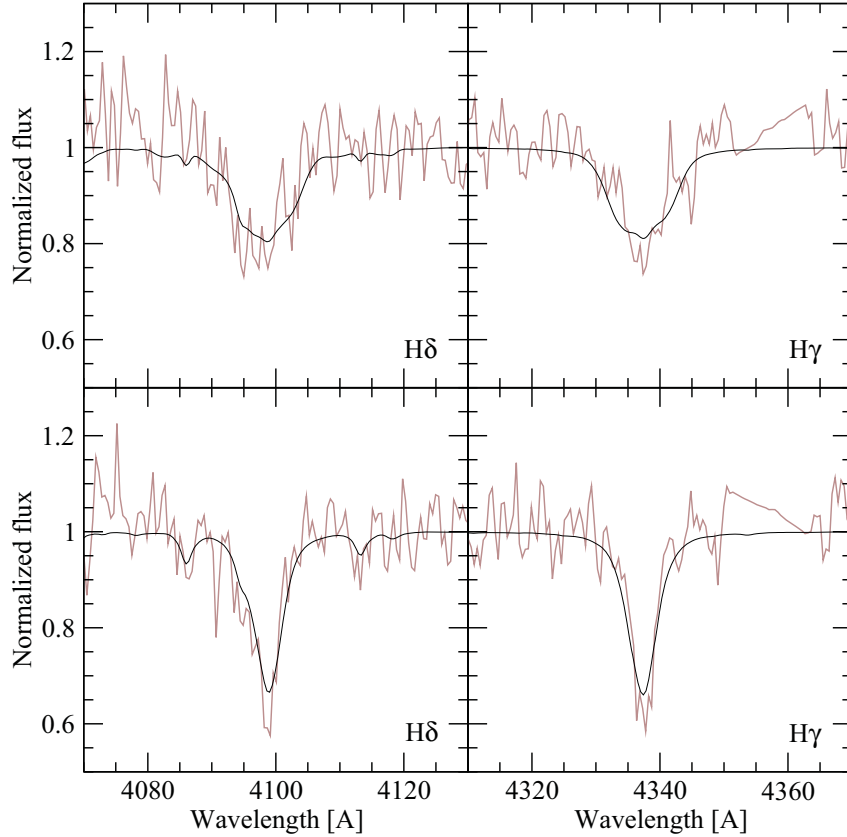| Time [HJD]	Phase	Primary [km s^{-1}]	Secondary [km s^{-1}]	Tertiary [km s^{-1}]
2 453 260.910	0.1728	-444±26	62±17	-190±10
2 453 295.776	0.2336	-465±19	59±23	-210±10
2 453 264.066	0.7214	27±23	-503±19	-241±10
2 453 321.820	0.7610	70±14	-500±20	-235±11
2 453 321.872	0.7699	86±18	-495±13	-221± 9

Figure 4.12. Balmer lines of M31V J00442326+4127082 (SB3) observed at two different orbital phases (0.23 top and 0.51 bottom). Gray lines correspond to the observed spectra and black lines correspond to the combination of three TLUSTY model spectra with the RVs, rotational velocities, luminosity ratios and surface gravities derived from the binary analysis (Sect. 4.1.4.2) and temperatures obtained from the comparison with stellar evolutionary models (Sect. 4.1.4.3).

ference is the number of attempted triplets of templates, somewhat lower, and the fact that only a single iteration was performed. The main reason for this is the large computational time required to obtain the RVs for each triplet of templates. The resulting RVs (Table 4.11) were corrected to the heliocentric reference frame (using standard IRAF routines) and rejected observations (after the W&D fit) are shown in Fig. 4.13. Again, all the rejected observations are close to the RV curve nodes or correspond to the spectrum with a shorter exposure time of February 2005.

4.1.4.2   Mass and radius determination

The RVs obtained for the two eclipsing components were used to derive their fundamental properties. The same procedure used for double-line EBs was followed,

Table 4.12. Fundamental properties of M31V J00442326+4127082 (SB3) derived from the analysis with W&D. Models of Lejeune & Schaerer (2001) were used for the tertiary.

System properties					
B magnitude at maximum light $(B_{\max})^a$		19.284±0.017			mag
V magnitude at maximum light $(V_{\max})^a$		19.195±0.014			mag
Period (P)		5.75268±0.00005			days
Time of minimum $(t_{\min})$		2 452 546.586±0.008			HJD
Eccentricity (e)		0.17±0.02			
Argument of periastron (ω)		45±7			deg
Time derivative of ω $(\dot{\omega})$		2.4±1.0			deg yr^{-1}
Inclination (i)		81.3±1.9			deg
Systemic velocity (γ)		-210±11			km s^{-1}
Semi-major axis (a)		62±2			R$_\odot$
Mass ratio $(q = \mathcal{M}_S/\mathcal{M}_P)$		0.94±0.07			
Temperature ratio $(T_{\text{eff},S}/T_{\text{eff},P})$		0.97±0.02			
Flux ratio in B $(F_{B,S}/F_{B,P})^a$		0.9±0.2			
Flux ratio in V $(F_{V,S}/F_{V,P})^a$		0.9±0.2			
Flux ratio in V_{DIRECT} $(F_{D,S}/F_{D,P})^a$		0.9±0.2			
Third light contribution in B $(l_{B,3})$		0.21±0.08			
Third light contribution in V $(l_{V,3})$		0.20±0.09			
Third light contribution in V_{DIRECT} $(l_{D,3})$		0.19±0.10			

Component properties	Primary		Secondary		Tertiary^c	
Radius (R)	15.3±1.3	R$_\odot$	14.7±1.3	R$_\odot$	11±3	R$_\odot$
Mass $(\mathcal{M})$	49±6	M$_\odot$	46±5	M$_\odot$	36±9	M$_\odot$
Surface gravity (log g in cgs)	3.76±0.07		3.77±0.08		3.92±0.10	
Radial velocity semi-amplitude $(K)^b$	263±15	km s^{-1}	279±15	km s^{-1}	—	
Synchronized rotational velocity $(v_{\text{sync}}\sin i)$	189±16	km s^{-1}	182±17	km s^{-1}	—	

^{a} Out of eclipse average: $\Delta\phi = [0.04 - 0.45, 0.63 - 0.88]$
^{b} Including non-Keplerian corrections
^{c} Assuming a single coeval component

providing fits with rms residuals of 0.018 mag in B, 0.013 mag in V and 0.033 mag for the DIRECT V light curve. The residuals of the RVs are 11 km s^{-1} and 15 km s^{-1} for the primary and secondary components, respectively. The light and RV curves, with their respective fits superimposed, are shown in Fig. 4.13.

The resulting best-fitting elements, listed in Table 4.12, reveal a detached EB with two components having masses (and radii) of $\mathcal{M}_P = 49\pm6$ M$_\odot$ ($R = 15.3\pm1.3$ R$_\odot$) and $\mathcal{M}_S = 46 \pm 5$ ($R = 17.7 \pm 1.3$ R$_\odot$) for the primary and secondary components, respectively. The derived values reveal that SB3 is an extremely massive and eccentric EB showing apsidal motion ($\dot{\omega} = 2.4 \pm 1.0$ deg year^{-1}). The synchronized rotational velocity shown in Table 4.12 was computed assuming pseudo-synchronization, where both components are synchronized at periastron angular velocity. All these quantities, together with additional properties, are further discussed in Sect. 4.1.4.3.

4.1.4.3 Comparison with stellar evolutionary models

The triple-line spectra obtained for SB3 could not be disentangled and, therefore, a direct temperature determination could not be obtained. However, considering
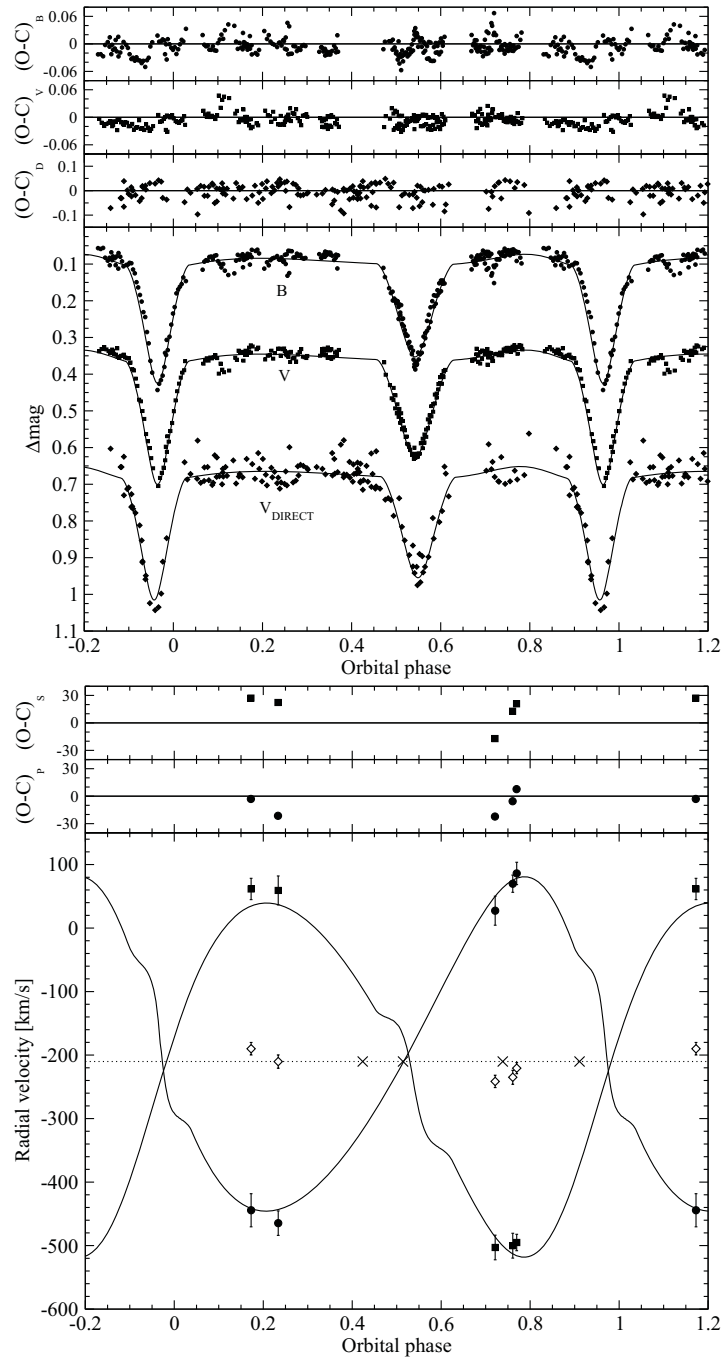
Figure 4.13. Observations for M31V J00442326+4127082 (SB3) and corresponding W&D fits. **Top:** Light curve fits and corresponding residuals. The residuals shown were derived for a mean epoch and do not consider the apsidal motion effect. **Bottom:** RV curve fits with RVs for the primary (circles), the secondary (squares) and the tertiary (empty diamonds) components, with corresponding residuals for the eclipsing components. Phases of rejected observations are also indicated (crosses).

Table 4.13. Fundamental properties of M31V J00442326+4127082 (SB3) derived from the comparison of the parameters in Table 4.12 with stellar evolutionary models of Lejeune & Schaerer (2001).

System properties						
Age				2.3±0.5		Myr
Absolute V magnitude (M_V)				-6.9±0.2		mag
Color excess ($E(B-V)$)				0.41±0.18		mag
Line-of-sight absorption (A_V)				1.3±0.6		mag
Distance modulus ($(m-M)_0$)				24.8±0.6		mag
Component properties	Primary		Secondary		Tertiary[a]	
Effective temperature (T_{eff})	40 000±2 000	K	40 000±2 000	K	39 000±3 000	K
Absolute V magnitude (M_V)	-5.93±0.17	mag	-5.82±0.20	mag	-5.1±0.5	
Intrinsic color ($(B-V)_0$)	-0.311±0.005	mag	-0.311±0.005	mag	-0.306±0.004	mag

[a] Assuming a single coeval component

that the eclipsing components are coeval, an accurate modeling of the system was obtained from comparison with stellar evolutionary models of Lejeune & Schaerer (2001).

As in previous cases, the mass-radius diagram was used to infer suitable evolutionary tracks with solar metallicity (Fig. 4.14). In this case, however, the detached nature of the system enabled us to assume that the components are coeval. In order to find the most likely coeval solution and the corresponding errors, a Monte Carlo simulation was performed with 1000 realizations. In addition to being coeval, the constraints derived from the W&D fits (i.e, temperature ratio, luminosity ratio and radius ratio) were also included. The resulting most likely models were used to determine the age, as well as the temperature and luminosity of both components (Table 4.13), revealing that both components are main sequence stars (Fig. 4.14).

The derived fundamental properties reveal a supermassive EB system, with the two components well above 40 $M_\odot$. In addition to determining the properties of the eclipsing components, the luminosity ratio could be used to infer the magnitude of the tertiary component. Considering the derived RVs of the tertiary component, it is reasonable to consider that all the stars belong to the same stellar association and are coeval. The resulting coeval absolute magnitude is $M_V = -5.1 \pm 0.5$ mag.

The large uncertainty in the computed M_V magnitude prevents a precise determination of other properties for the tertiary component. In addition, the third light contribution could be due to one or several stars. However, to explain the relatively bright M_V magnitude, the tertiary component has to be composed by one (or several) hot stars (i.e., $T_{\mathrm{eff}} > 30 000$ K). To further confirm this scenario, a synthetic spectrum was generated with three equal stars (with the properties inferred from the binary analysis) and compared to the observed spectra (Fig. 4.12). After some attempts, it was observed that the rotational velocity of the tertiary component had to be rather low (40 km s^{-1} in Fig. 4.12) to reproduce the observed line depths. In
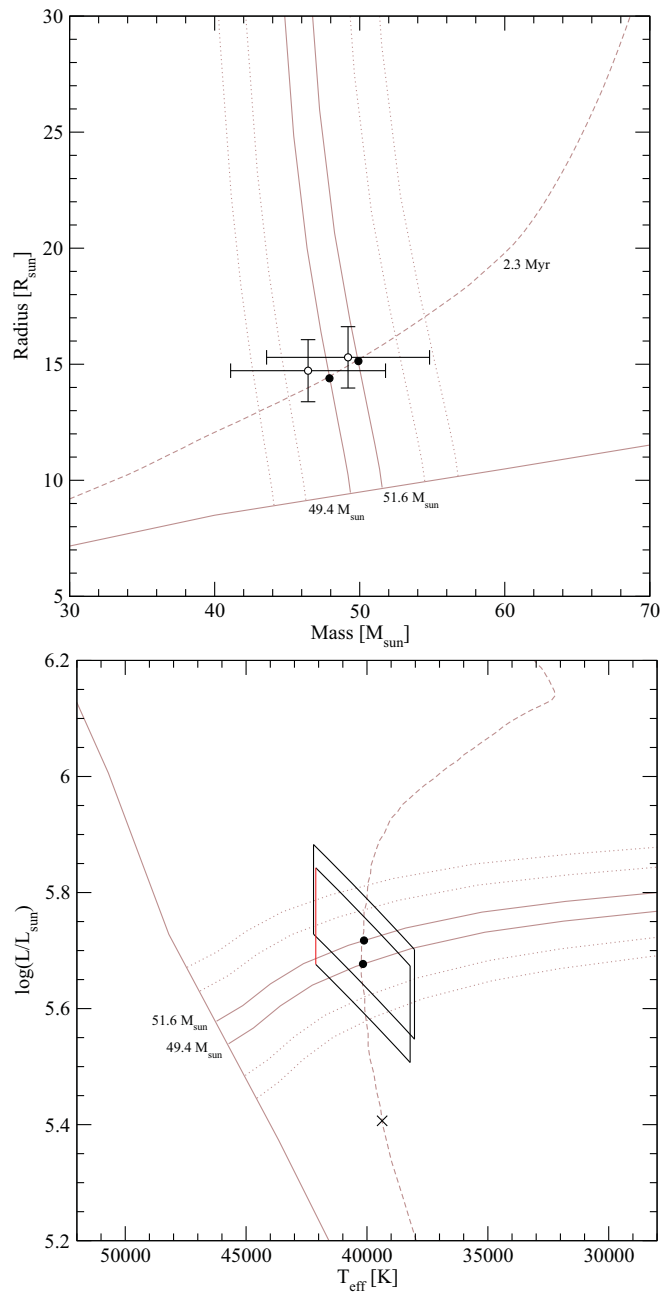
Figure 4.14. Comparison of stellar evolutionary models with derived physical properties of M31V J00442326+4127082 (SB3). Results obtained after the W&D fitting are shown (open circles) together with the most likely coeval solution (black circles). Gray solid lines correspond to the ZAMS and the evolutionary tracks (initial masses are labeled). The best fitting isochrone of 2.3 Myr is also shown (gray dashed line). Gray dotted lines denote the uncertainties in the derived masses. **Top:** Mass–radius diagram. **Bottom:** H-R diagram. The skewed rectangular boxes correspond to 1σ error loci. The coeval position of the tertiary source is also shown (cross).

any case, the combined spectra seem to be capable of reproducing the observed shapes of the lines rather well considering the noise of the observed spectra.

The most distinctive characteristic of SB3 is the large measured apsidal motion. The measured value of $\dot{\omega} = 2.4 \pm 1.0$ deg year^{-1}, in combination with the derived masses, converts SB3 into the most massive EB system with measured apsidal motion ever reported. The measured apsidal motion rate can be compared with theoretical predictions and will be subject of future investigation. So far, three possible causes can be put forward to explain the observed apsidal motion (see Guinan & Maloney, 1985, for details).

Firstly, the presence of a third body can introduce an apsidal motion (together with additional effects, for instance in the inclination). However, even supposing that the third body is tidally bound, forming a triple system with the EB, the derived RVs for the tertiary component reveal that the rotational period of the supposed triple system is much longer (> 100 times longer) than the EB period. Since the angular motion rate depends on the ratio of periods as $(P/P')^2$, where P is the EB period and P' is the triple system period, the effect of the third body on the apsidal motion has to be several orders of magnitude lower than the observed value.

Secondly, general relativity introduces an advance in the periastron that, for some EB systems, is large enough to be observed. In this case, however, the relativistic effect introduced in the apsidal motion is on the order of 0.2–0.3 deg yr^{-1}, much lower than the observed apsidal motion.

Finally, the most likely cause for the observed apsidal motion is due to the deformation of the components. The apsidal motion rate depends on the eccentricity of the EB system, the relative radius of the components, the mass ratio, the period and rotational velocity (Claret & Gimenez, 1993). In addition, the distribution of matter in the interior of the stars (modeled as internal structure constants, k_2) are critical values to determine the apsidal motion rate. Using the values tabulated in Claret (2004), the internal structure constants derived for the primary and the secondary components are $\log k_{21} = -2.44 \pm 0.16$ and $\log k_{22} = -2.52 \pm 0.17$. These values, when combined with the parameters derived from the binary analysis (Table 4.12) and assuming pseudo-synchronization, result in a predicted apsidal motion rate of $\dot{\omega}_{\text{theo}} = 5.4 \pm 0.8$ deg year^{-1} or, equivalently, a period of apsidal revolution of $U_{\text{theo}} = 66 \pm 10$ years. This value is discordant (at the 2σ level) with the observed apsidal motion rate of $\dot{\omega} = 2.4 \pm 1.0$ deg year^{-1} ($U = 150 \pm 60$ years). The same situation is observed for other B stars with convective cores (e.g., V380 Cyg and CO Lac Guinan, 1993; Guinan et al., 2000). The general explanation for the observed discrepancy is that the internal structure constants predicted by the stellar evolution models are too large, implying too small convective cores. Therefore, the observed apsidal motion rate seems to support the idea that the internal structure constants predict cores that are too small when compared with observations. In any case further analysis is needed to better ensure that the ob-

Table 4.14. Distance determinations to M 31 from EBs.

EB system	V [mag]	M_V [mag]	A_V [mag]	$(m - M)_0$ [mag]	Distance [kpc]
SB2A	19.27±0.02	-5.77±0.06	0.60±0.10	24.44±0.12	772±44
SB2B	19.948±0.015	-4.90±0.08	0.55±0.08	24.30±0.11	724±37
SB3	19.195±0.014	-6.9±0.2	1.3±0.6	24.8±0.6	910±250

served apsidal motion is caused by the internal structure of their components and not by other factors (such as a tertiary component).

As a final remark, it is worth mentioning that absolute magnitudes could be derived from the comparison with stellar evolutionary models. Therefore, the derived luminosities could be used to obtain a line-of-sight absorption and a distance modulus to M 31 (Table 4.13), revealing a highly reddened system. The large uncertainty in the third light contribution, combined with the unknown total-to-selective extinction ratio ($\mathcal{R}_V$), makes that the derived distance is highly uncertain. In any case, the resulting distance is within one sigma of the direct distance determinations obtained with SB2A and SB2B (Sect. 4.1.1 and Sect. 4.1.2) and further confirms the scenario described for SB3.

4.2 Distance determination

From the four analyzed EBs, three of them have provided a distance determination to M 31 (Table 4.14). As previously mentioned (Sect. 4.1.1.3), the derived distances to each EB correspond to the center of M 31, because the correction due to the location of the EB is negligible ($\sim 0.3\%$). Therefore, the derived distances, in mutual agreement within their one sigma error bars, prove that EBs can be used to derive precise and accurate distances to M 31.

The derived distances can be averaged to derive a robust distance to M 31. Of the three distance determinations, only two can be considered direct distance determination. The distance value of SB3 cannot be considered to be direct because it is based on stellar evolutionary models. As it is well known, stellar evolutionary models depend on a certain number of assumptions that can affect the derived distance (mass loss, rotational velocity, isolated stellar evolution, etc.). In any case, the large error associated with the distance to SB3 makes that the weighted mean value would vary only slightly if the SB3 distance determination is included. Therefore, the two double-line EBs have been combined to derive a weighted mean distance to M 31 of 744 ± 33 kpc or $(m - M)_0 = 24.36 \pm 0.08$ mag. Although additional EBs are needed to increase the statistical significance, the derived result has an error of only 4%, which is remarkable, given the faintness of the studied targets.

Note that the error bars account for the random uncertainties of the parameters but do not include a possible systematic contribution from the atmosphere models. However, stellar atmosphere models are used in a large number of applications and have been tested thoroughly in several research areas. In addition, our spectrophotometric measurements are fully compatible with stellar atmosphere models, reducing the possibility of important systematics in the models. Therefore, we expect such systematic error to be no larger than a few per cent in flux, having an effect below 0.05 mag in the distance modulus.

Another possible source of systematic error is the fact that both EBs used for distance determination are modeled as semi-detached systems. It has traditionally been argued that detached EBs are the only systems capable to provide accurate distances. The most common reason is that non-detached EBs are affected by the proximity of the components, introducing distortions and reflection effects. However, the proximity of the components can properly be taken into account by current modeling algorithms (such as W&D). In addition, the fact that one of the components fills the Roche lobe decreases the number of free parameters and greatly improves the stability of the solution (Wyithe & Wilson, 2002). On the other hand, there are some other effects, missing in detached EB, that could introduce some systematics in the solutions (e.g., hot spots, circumstellar disks, etc.). In any case, these effects can be observed from the acquired data and properly taken into account. A clear example of these effects is the presence of the O'Connell effect in SB2A. The modeling performed, with the introduction of a hot spot, has been capable to accurately consider this effect, allowing the use of SB2A for distance determination. Therefore, using semi-detached EBs reduces the number of free parameters, at the cost of introducing some other effects that, when properly considered, should introduce no systematic error in the derived distances.

It is also important to remark that the procedure used in the present work, although resource-intensive, is completely independent of any other distance determination. Therefore, with this procedure, distance determination is both highly precise and direct. In addition, without the need for spectrophotometry, the observational requirements decrease, which greatly simplifies the procedure and opens the possibility to perform distance determinations for a large number of EBs.

The need for spectrophotometry could be circumvented because we derived T_{eff} from the disentangled spectra and benefit from the weak temperature dependency of $(B - V)$ above ~ 30000 K to obtain an $E(B - V)$ value. The major cost of loosing spectrophotometric information is an increase in the line-of-sight absorption uncertainty. In fact, uncertainty in the extinction represents $\sim$50% of the total error in the distance determination. Therefore, any further improvements that reduced the uncertainty in the line-of-sight absorption could potentially improve the distance determinations presented here.